

New insights of heterogeneous nucleation and anisotropic growth of acicular ferrite on non-metallic inclusion

Changji Xuan ^{a,*}, Wangzhong Mu ^{b,*}

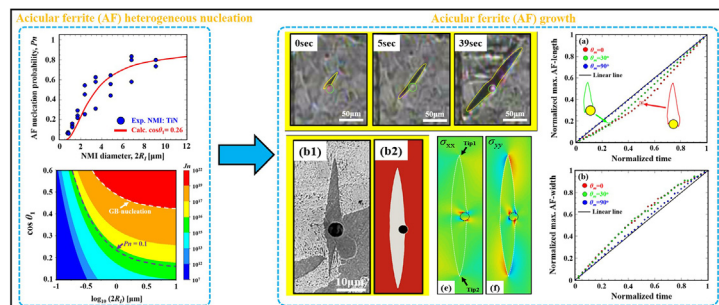
^a Sandvik Manufacturing Solutions AB, Additive Manufacturing Division, SE-811 81 Sandviken, Sweden

^b KTH Royal Institute of Technology, Department of Materials Science and Engineering, Brinellvägen 23, Stockholm SE-100 44, Sweden

HIGHLIGHTS

- The model for the first time reasonably describes the acicular ferrite (AF)-nucleation probability.
- An interaction map which quantitatively reveals influences of the interfacial energies and NMI-size on the AF-nucleation potency is quantitatively established.
- It for the first time reveals that the misorientation angle between the favorable growth direction and normal vector influences the AF-evolution behavior.
- The anisotropic stress field induced by such interaction leads to the irregular AF-deformation near NMI.

GRAPHICAL ABSTRACT



ARTICLE INFO

Article history:

Received 16 May 2022

Revised 21 June 2022

Accepted 22 June 2022

Available online 27 June 2022

Keywords:

Heterogeneous nucleation
Phase transformation
Acicular ferrite
Interfacial energy
Anisotropic precipitation
Modeling

ABSTRACT

This work studies the acicular ferrite (AF) nucleation and growth from a classical defect, i.e. non-metallic inclusion surface. The heterogeneous AF-nucleation probability on NMI is predicted by a mathematical model following the classical nucleation theory. The calculation results are in consistent with the experimental data. The current model includes the exact form of the activation energy and Zeldovich factor for heterogeneous nucleation on pre-existing spherical surface. It generates an interaction map that for the first time quantitatively describes the superposition influences of the interfacial energies and NMI-size on the AF-nucleation potency. In the AF-growth aspect, we systematically reveal the single AF-plate evolution behavior through the synergy between the experimental observations and multiphase-field simulations. It is found that the AF-tip morphology is impacted by the misorientation angle between the favorable growth direction and normal vector. It also influences the AF-lengthening and widening kinetics. Additionally, the anisotropic stress field induced by the AF-NMI interface plays a significant role in controlling the complex curvature of the AF-plate. The current study opens new perspectives for understanding the AF-precipitation mechanisms.

© 2022 The Authors. Published by Elsevier Ltd. This is an open access article under the CC BY license (<http://creativecommons.org/licenses/by/4.0/>).

1. Introduction

Phase transformation in the region of metastability can be initiated within the original phase by the nucleation of small regions of the new phase. In particular, solid phase transformation from the

* Corresponding authors.

E-mail addresses: xuanchangji@msn.com (C. Xuan), wmu@kth.se (W. Mu).

matrix has been widely employed in the design and manufacturing process of materials. This transformation will be crucial for the microstructure evolution in the related materials which can achieve desired properties [1–2]. Nucleation and growth are two vital steps for one phase formation (nucleus) from another one (matrix). Generally speaking, the majority of new solid phase transformation prefers a heterogeneous nucleation process, which needs a much lower driving force than that for a homogeneous nucleation. The heterogeneous nucleation normally involves the distribution control of heterogeneities, i.e. defects [3], for example non-metallic inclusion (NMI) in metals. These are considered as the favorable nucleation sites for new phase formation.

The above-mentioned solid phase transformation almost exists in all kinds of engineering materials. Among different types of microstructure evolution, acicular ferrite (AF) is a typical microstructure that precipitates in the interior of the original γ austenite-grain through the heterogeneous nucleation on non-metallic inclusions (NMIs). Although the 'acicular' term denotes a needle-like morphology, it has been experimentally confirmed that AF is in form of a lenticular plate with very thin thickness rather than a rod [4] (see Fig. 1). Due to its chaotic ordering leading to a fine 'basket weave' appearance, the material microstructure achieves a considerable improvement in strength and toughness [5–6]. Since 1970s, much efforts have been devoted to evaluate the influences of different factors (e.g. γ grain size [7–9], cooling rate [10], steel composition [11], NMI types [12–15], etc) on the AF-formation behavior. However, more work is still required to better understand the AF-nucleation mechanism and transformation kinetics.

It is generally recognized that AF is essentially intragranular bainite [16]. In addition, the AF morphology differs significantly from Widmanstätten microstructure with a series of parallel plates precipitating from γ grain boundaries (GBs). The high formation similarity of these two microstructures results in a nucleation competition. Using Fletcher theory [17], Ricks et al. [18] estimated the activation energy for the AF-nucleation by setting an equal interfacial energy between the NMI- γ austenite ($\sigma_{I\gamma}$) and NMI- α ferrite (σ_{Ix}) interfaces. It was demonstrated that GBs always act as more favorable nucleation sites, compared with NMI. In contrast, Madariaga and Gutierrez [19] selected different $\sigma_{I\gamma}$ and σ_{Ix} values, and proposed that the nucleation potency of NMI will be larger than that of GB if the contact angle of nucleus with respect to the precipitation interface (θ_1 in this work) exceeds a certain degree. Despite diverse conclusions, both groups relied on the

assumptions of interfacial energies. A more comprehensive analysis is needed to rationalize such comparison. More recently, Mu et al. [15] followed the same concept but used realistic interfacial energies to assess critical NMI-size for the AF-nucleation. Several experimental works [20–23] reported the growth of the AF-nucleation probability with the increased NMI-size. This phenomenon can be well explained by Ricks model [18], which shows that larger NMI lowers the activation energy. Nevertheless, no research further developed this approach to directly predict such AF-kinetic information as the nucleation rate or nucleation probability. Babu and David [24] attempted to apply a bainite model [25] to describe the degree of the AF-transformation. Although the nucleation rate was estimated in a case study, their methods are purely based on a fitting process to the experimental data rather than fundamental knowledge of nucleation theory [26]. In addition, the NMI-size as one of the key factors for AF is not included in the original bainite model. According to previous studies, there may be a relation coupling the influences of the interfacial energy and NMI-size on the AF-nucleation potency. However, this general pattern has not been fully clarified so far.

When the $\gamma \rightarrow \alpha$ transformation occurs after the α -nucleation, the α phase exhibits a strong anisotropy-growth along the habit plane upon cooling [9] or under isothermal conditions [27]. The interface anisotropy depends on the interface-boundary orientation as well as the relatively crystallographic orientation of two neighbor phases. Although high strain energy near NMI was reported [26], the impact of the AF-NMI interface interaction on the AF-precipitation behavior remains unclear. The nucleation position at NMI, in principle, may also influence the AF-plate evolution. If its favorable growth direction (FGD) is parallel to the normal vector, the plate will most likely follow an epitaxial growth. On the other hand, if the former has a misorientation angle with the later one, the plate might have different evolution pathway. Such hypothesis can be partially supported by experimental observations in literature [28–30] although no related analysis was mentioned in previous researches. To the authors' best knowledge, a detailed study about the influence of the misorientation of favorable growth direction (FGD) on the AF-evolution has not been reported before.

The aim of the present work is thus to take insight into the open questions stated-above. The kinetics of the AF-nucleation and growth on NMI is studied in-depth. In Section 2, the heterogeneous AF-nucleation is systematically evaluated by developing a mathematical model within the classical nucleation framework. The model is validated using the measured experimental data of nucleation probabilities. The superposition influences of the interfacial energy and NMI-size on the AF nucleation potency are, for the first time, established through an interaction map. In Section 3, we systematically describe the evolution mechanism of the AF single plate by coupling the experimental observations and multiphase-field modeling (PFM). As mentioned, the impact of the AF evolution on the interface migration is rather complicated. To track the strong anisotropy of microstructure, the current PFM model incorporates the anisotropy contributions of both the interfacial energy and long-range elastic energy.

2. Kinetics of AF-nucleation

In the current analysis, the physical basis of the AF-nucleation kinetics on NMI (AF-NMI) follows the Becker-Döring law [31]. It is needed to determine rigorous forms of two crucial terms as the critical nucleation energy, ΔG^* and Zeldovich factor, Z . The homogeneous nucleation (HN) and heterogeneous grain-boundary-nucleation (HGBN) are also involved for the theory continuity and ease of comparison. As a normal method in the classical

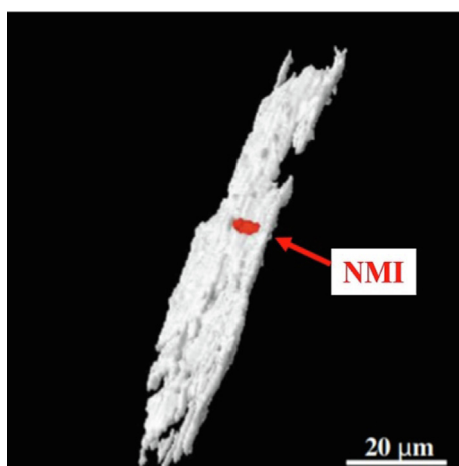


Fig. 1. 3D-reconstructed image of AF. Reproduced with permission [4]. Copyright 2009, Elsevier.

nucleation theory (CNT), it is assumed that the nucleus - and NMI-morphologies are spherical/partially spherical, as is schematically illustrated in Fig. 2. This hypothesis indicates that the elastic energy contribution can be negligible, compared with the interface one in the incubation period. If the elastic contribution becomes significant, the precipitate will strongly deviate from a sphere and show an anisotropic growth. Such kinetic behavior during the AF growth will be discussed in Section 3 in detail.

2.1. Derivation of critical nucleation energy

The overall energy barrier for nucleation is composed of the bulk free energy (ΔG_V) and interfacial energy (ΔG_A) contributions, and reads,

$$\Delta G = \Delta G_V + \Delta G_A = \Delta F_{chem} V_\alpha + \Delta G_A \quad (a1)$$

where ΔF_{chem} is the chemical driving force, V_α is the nucleus volume, and ΔG_A is the interfacial energy contribution. In the homogeneous nucleation case (see Fig. 2(a)), Eq. (a1) is expanded to,

$$\Delta G = \frac{4}{3}\pi R_\alpha^3 \Delta F_{chem} + 4\pi R_\alpha^2 \sigma_{xy} \quad (a2)$$

where R_α and σ_{xy} denote the equivalent-nucleus radius and interfacial energy between the α and γ phases, respectively. The nucleation takes place when ΔG reaches its maximum value where $\frac{\partial(\Delta G)}{\partial R_\alpha} = 0$. Taking partial differential, the well-known expressions of the criti-

cal nucleation radius, R_α^* and corresponding energy, ΔG_{hom}^* change are achieved as,

$$R_\alpha^* = -\frac{2\sigma_{xy}}{\Delta F_{chem}} \quad (a3)$$

$$\Delta G_{hom}^* = \frac{16\pi\sigma_{xy}^3}{3\Delta F_{chem}^2} \quad (a4)$$

Here, Fe-0.2 wt% C was selected as an example since this is one of the basic and vital engineering material systems. The chemical driving force calculated with Thermo-Calc ($=-0.44 \times 10^8 \text{ J/m}^3$ at 973 K) has a same order of magnitude as the experimental measurements [32]. Nevertheless, applying the reported σ_{xy} ($=0.75 \text{ J/m}^2$ [18]), the estimated R_α^* value through Eq. (a3) equals 34 nm, which is tremendously larger than the common AF-nucleus size ($\sim 0.15\text{--}0.5 \text{ nm}$ [33]). Here, a reasonable R_α^* value ($=0.4 \text{ nm}$) is initially fixed, and a correction factor, k_1 ($=85.2$) is introduced into Eq. (a1) to ensure the capability of nucleation theory,

$$\Delta G = k_1 \Delta F_{chem} V_\alpha + \Delta G_A \quad (a5)$$

and then Eqs. (a3)-(a4) are re-written as

$$R_\alpha^* = -\frac{2\sigma_{xy}}{k_1 \Delta F_{chem}} \quad (a6)$$

$$\Delta G_{hom}^* = \frac{16\pi\sigma_{xy}^3}{3k_1^2 \Delta F_{chem}^2} \quad (a7)$$

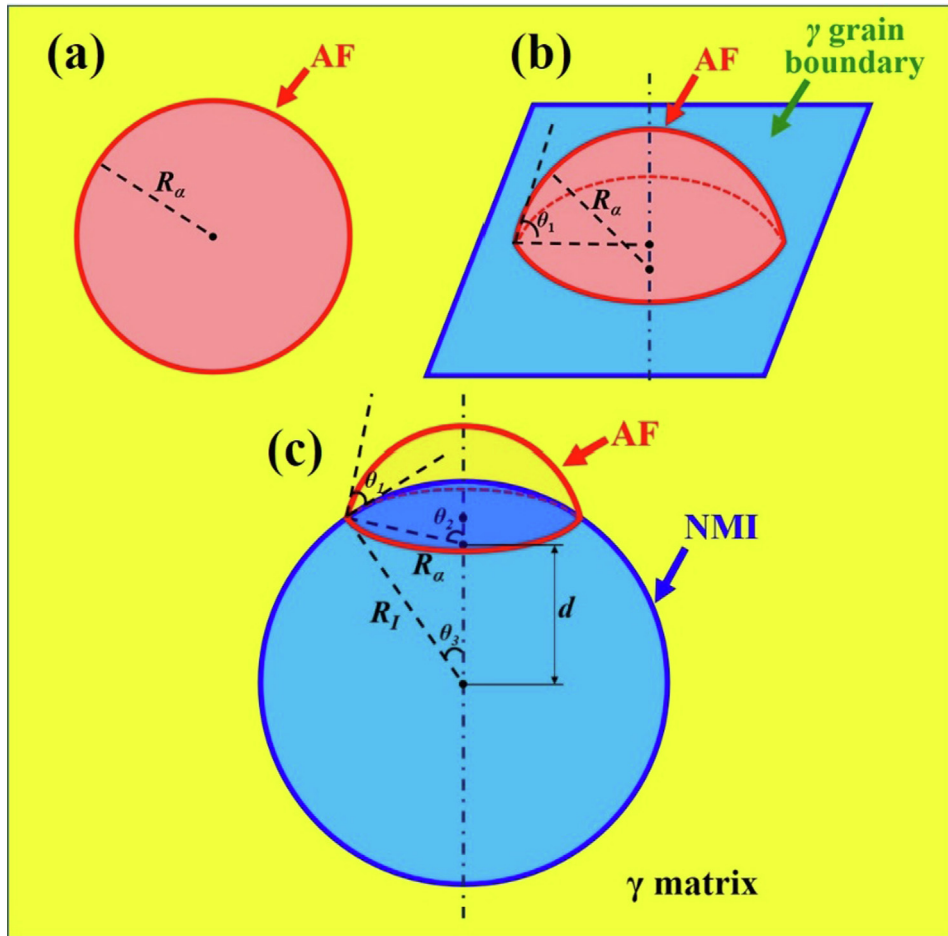


Fig. 2. Schematic illustration of (a) homogeneous AF-nucleation (HN); (b) heterogeneous AF-grain-boundary-nucleation (HGBN); (c) heterogeneous AF-nucleation on NMI (AF-NMI).

When a nucleus heterogeneously precipitates on a grain boundary, its morphology can be approximated with a cap-shape model (see Fig. 2(b)). The nucleating AF generates a cap that is in contact with the underlying GB. It introduces the contact angle (θ_1) of nucleus with respect to the precipitation interface. Based on the mechanical equilibrium in terms of interfacial energies, following equation is obtained as,

$$\cos\theta_1 = (\sigma_{\gamma\gamma} - \sigma_{x\gamma})/\sigma_{x\gamma} \quad (a8)$$

where $\sigma_{\gamma\gamma}$ is the surface energy of the γ phase ($=1.04 \text{ J/m}^2$ [18,34]). Then, Eq. (a5) is expanded to,

$$\Delta G = k_1 \Delta F_{chem} V_\alpha + [\sigma_{x\gamma} \cdot A_{x\gamma} + (\sigma_{x\gamma} - \sigma_{\gamma\gamma}) \cdot A_{\alpha-boundary}] \quad (a9)$$

where $A_{x\gamma}$ and $A_{\alpha-boundary}$ are contact areas of the α - γ phases and α -grain boundaries, respectively. Based on the geometry relations, following equations are established as,

$$V_\alpha = \frac{\pi}{3} R_\alpha^3 (2 + \cos\theta_1)(1 - \cos\theta_1)^2 \quad (a10)$$

$$A_{x\gamma} = 2\pi R_\alpha^2 (1 - \cos\theta_1) \quad (a11)$$

$$A_{\alpha-boundary} = \pi R_\alpha^2 \sin\theta_1^2 \quad (a12)$$

Substituting Eqs. (a8), (a10)-(12) into Eq. (a9) yields,

$$\Delta G = \left(\frac{4}{3} \pi R_\alpha^3 k_1 \Delta F_{chem} + 4\pi R_\alpha^2 \sigma_{x\gamma} \right) \cdot \frac{(2 + \cos\theta_1)(1 - \cos\theta_1)^2}{4} \quad (a13)$$

Taking differential of Eq. (a13), the critical nucleation energy, ΔG_{het}^* is given by,

$$\Delta G_{het}^* = \Delta G_{hom}^* \cdot \frac{(2 + \cos\theta_1)(1 - \cos\theta_1)^2}{4} \quad (a14)$$

It needs to mention that the expression of the critical nucleation radius, R_α^* is the same as Eq. (a6). If a spherical NMI acts as the heterogenous nucleation site (see Fig. 2(c)), Eq. (a5) will be expanded to,

$$\Delta G = k_1 \Delta F_{chem} V_\alpha + [\sigma_{x\gamma} \cdot A_{x\gamma} + (\sigma_{I\gamma} - \sigma_{Ix}) \cdot A_{Ix}] \quad (a15)$$

where $\sigma_{I\gamma}$ and σ_{Ix} are the interfacial energies of the NMI- γ phases and NMI- α phases, respectively. A_{Ix} represents the contact area of the NMI- α phases. According to the geometry relations in Fig. 2 (c), following equations are obtained,

$$\cos\theta_1 = (\sigma_{I\gamma} - \sigma_{Ix})/\sigma_{x\gamma} \quad (a16)$$

$$d = (R_I^2 + R_\alpha^2 - 2R_I R_\alpha \cos\theta_1)^{0.5} \quad (a17)$$

$$\cos\theta_2 = (R_I \cos\theta_1 - R_\alpha)/d \quad (a18)$$

$$\cos\theta_3 = (R_I - R_\alpha \cos\theta_1)/d \quad (a19)$$

$$A_{x\gamma} = 2\pi R_\alpha^2 (1 - \cos\theta_2) \quad (a20)$$

$$A_{Ix} = 2\pi R_I^2 (1 - \cos\theta_3) \quad (a21)$$

$$V_\alpha = \frac{\pi}{3} R_\alpha^3 (2 + \cos\theta_2)(1 - \cos\theta_2)^2 - \frac{\pi}{3} R_I^3 (2 + \cos\theta_3)(1 - \cos\theta_3)^2 \quad (a22)$$

Coupling Eqs. (a16)-(a22) into Eq. (a15) and making differential, the critical nucleation energy, ΔG_{het}^* reads

$$\Delta G_{het}^* = \Delta G_{hom}^* \cdot f(\theta_1, \tau) \quad (a23)$$

$$f(\theta_1, \tau) = 0.5 + 0.5 \left(\frac{1 - \tau \cdot \cos\theta_1}{\varphi} \right)^3 + \left[1 - 1.5 \left(\frac{\tau - \cos\theta_1}{\varphi} \right) + 0.5 \left(\frac{\tau - \cos\theta_1}{\varphi} \right)^3 \right] \cdot \tau^3 - 1.5 \cos\theta_1 \tau^2 \left[1 - \left(\frac{\tau - \cos\theta_1}{\varphi} \right) \right] \quad (a24)$$

$$\tau = \frac{R_I}{k_2 R_\alpha^*} \quad (a25)$$

$$\varphi = (1 - 2\tau \cdot \cos\theta_1 + \tau^2)^{0.5} \quad (a26)$$

In previous work [15], Eq. (a23) was merely applied for a qualitatively theoretical discussion. To achieve the realistic application by comparing with experiments, one adjustable factor, k_2 ($=400$) is suggested to be introduced (see Eq. (a25)). It is used to control the R_I susceptibility on nucleation. It needs to mention that k_2 is independent of the NMI type variation. Although R_α^* cannot be analytically solved by Eq. (a15), it is reasonable to apply Eq. (a6) for the approximation [17].

2.2. Derivation of Zeldovich factor

The Zeldovich factor, Z describes the cluster fluctuations around the critical nucleation size and the redissolution probability of a stable nucleus. Its general expression is by definition [35],

$$Z = V_p \left(-\frac{1}{2\pi kT} \frac{\partial^2 \Delta G}{\partial (V_\alpha)^2} \Big|_{R_\alpha=R_\alpha^*} \right)^{0.5} \quad (a27)$$

where V_p is the atomic volume of the α phase, and k represents the Boltzmann constant. Using Eq. (a5), the first- and second-partial differential expressions of ΔG by V_α are rearranged as,

$$\frac{\partial \Delta G}{\partial V_\alpha} = k_1 \Delta F_{chem} + \frac{\partial \Delta G_A}{\partial R_\alpha} \cdot \left(\frac{\partial V_\alpha}{\partial R_\alpha} \right)^{-1} \quad (a28)$$

$$\frac{\partial^2 \Delta G}{\partial (V_\alpha)^2} = \frac{\partial^2 \Delta G}{\partial V_\alpha \partial R_\alpha} \cdot \left(\frac{\partial V_\alpha}{\partial R_\alpha} \right)^{-1} \quad (a29)$$

In the HN case, the functional derivatives of ΔG_A and V_α with respect to R_α are given by

$$\frac{\partial \Delta G_A}{\partial R_\alpha} = 8\pi \sigma_{x\gamma} R_\alpha; \frac{\partial V_\alpha}{\partial R_\alpha} = 4\pi R_\alpha^2 \quad (a30)$$

Substituting Eq. (a30) into Eqs. (a28)-(a29), the explicit Z form in Eq. (a27) is written as,

$$Z_{hom} = \frac{V_p}{2\pi R_\alpha^{*2}} \left(\frac{\sigma_{x\gamma}}{kT} \right)^{0.5} \quad (a31)$$

For the HGBN case (using Eqs. (a9)-(a10)), Eq. (a30) is re-expressed by,

$$\frac{\partial \Delta G_A}{\partial R_\alpha} = 2\pi \sigma_{x\gamma} R_\alpha (2 + \cos\theta_1)(1 - \cos\theta_1)^2 \quad (a32)$$

$$\frac{\partial V_\alpha}{\partial R_\alpha} = \pi R_\alpha^2 (2 + \cos\theta_1)(1 - \cos\theta_1)^2 \quad (a33)$$

Inserting Eqs. (a28), (a32)-(a33) into Eq. (a29), we obtain the second functional derivative of ΔG as,

$$\frac{\partial^2 \Delta G}{\partial (V_\alpha)^2} = \left(\frac{-2\sigma_{x\gamma}}{\pi R_\alpha^4} \right) (2 + \cos\theta_1)^{-1} (1 - \cos\theta_1)^{-2} \quad (a34)$$

Combining Eq. (a27), (a31) and Eq. (a34) yields the corresponding Zeldovich factor,

$$Z_{het} = Z_{hom} \cdot [2(2 + \cos\theta_1)^{-0.5}(1 - \cos\theta_1)^{-1}] \quad (\text{a35})$$

In the AF-NMI case (using Eq. (a15) and Eq. (a22)), Eq. (a30) is re-written as,

$$\frac{\partial \Delta G_A}{\partial R_\alpha} = 2\pi\sigma_{xy}R_\alpha \left[2 + \frac{(P^3 - 3P)\tau^3 + 3(P^2 + 1)\tau^2 - 6P\tau + 2}{(\tau^2 - 2P\tau + 1)^{1.5}} \right] \quad (\text{a36})$$

$$\frac{\partial V_\alpha}{\partial R_\alpha} = \pi R_\alpha^{-2} \left[2 + \frac{(P^3 - 3P)\tau^3 + 3(P^2 + 1)\tau^2 - 6P\tau + 2}{(\tau^2 - 2P\tau + 1)^{1.5}} \right] \quad (\text{a37})$$

$$P = \cos\theta_1 \quad (\text{a38})$$

The second functional derivative of ΔG hence becomes

$$\frac{\partial^2 \Delta G}{\partial (V_\alpha)^2} = \left(\frac{-2\sigma_{xy}}{\pi R_\alpha^4} \right) \left[2 + \frac{(P^3 - 3P)\tau^3 + 3(P^2 + 1)\tau^2 - 6P\tau + 2}{(\tau^2 - 2P\tau + 1)^{1.5}} \right]^{-1} \quad (\text{a39})$$

Applying Eq. (a31) and Eq. (a39), the explicit Zeldovich factor reads,

$$Z_{het} = Z_{hom} \cdot \left[0.5 + \frac{(P^3 - 3P)\tau^3 + 3(P^2 + 1)\tau^2 - 6P\tau + 2}{4(\tau^2 - 2P\tau + 1)^{1.5}} \right]^{-0.5} \quad (\text{a40})$$

2.3. Nucleation rate and probability

The stationary nucleation rate is given by a standard Becker-Döring law [31]

$$J_n = N_0 Z \beta^* \exp\left(-\frac{\Delta G^*}{kT}\right) \left(1 - \exp\left(-\frac{t^*}{t_0}\right)\right) \quad (\text{a41})$$

$$\beta^* = \frac{4\pi R^2 D_c^\gamma C_0}{a_\gamma^4} \quad (\text{a42})$$

N_0 is the number of atoms by unit atomic volume ($=1/V_p$, $V_p = 1.6 \times 10^{-29} \text{ m}^3$), β^* is the condensation rate of solute atoms in a cluster of critical size R^* , k is the Boltzmann constant, $t_0 = 1/(2\beta^*Z)$ denotes the incubation time of nucleation, t^* is the characteristic nucleation time ($=1.9 \times 10^{-17} \text{ s}$), D_c^γ is the diffusion coefficient of carbon in the matrix ($=3.6 \times 10^{-13} \text{ m/s}^2$ [36]), C_0 is the initial carbon molar content in the matrix, a_γ is the lattice constant of the γ phase ($=0.354 \text{ nm}$ [37]). The nucleation probability, P_n for one condensation nucleus is expressed as [38],

$$P_n = 1 - \exp(-J_n t^*) \quad (\text{a43})$$

The applied parameters for the simulation are summarized in Table 1. In subsequent section, we intend to use J_n and P_n to evaluate the AF-nucleation potency.

2.4. Evaluation of nucleation potency

To validate the theoretical consideration, the predicted AF-nucleation probabilities (P_n) are compared with the experimental results, as is shown in Fig. 3. Experimental data of P_n with each inclusion size of d_i was calculated using the number of nuclei inclusions ($N_{nu,i}$) divided by the number of total inclusions ($N_{total,i}$) with

Table 1
Physical parameters applied in AF-nucleation model.

Symbol	Definition and unit	Value
T	Temperature [K]	973
ΔF_{chem}	Chemical driving force [J/m ³]	-4.4×10^7
σ_{xy}	Interfacial energy between α and γ [J/m ²]	0.75 [18]
σ_{yy}	Surface energy of γ [J/m ²]	1.04 [18,34]
σ_{ly}	Interfacial energy between NMI and γ [J/m ²]	0.636 (TiN) [39], 0.842 (TiO _x) [15]
σ_{lx}	Interfacial energy between NMI and α [J/m ²]	0.439 (TiN) [39], 0.53 (TiO _x) [15]
k_1, k_2	Correction factor	85.2; 400
V_p	Unit atomic volume [m ³]	1.16×10^{-29}
t^*	Characteristic nucleation time [s]	1.9×10^{-17}
D_c^γ	Diffusion coefficient of carbon in the matrix [m/s ²]	3.6×10^{-13}
C_0	Initial carbon molar content in matrix	0.0093
a_γ	Lattice constant of γ [m]	0.354×10^{-9}

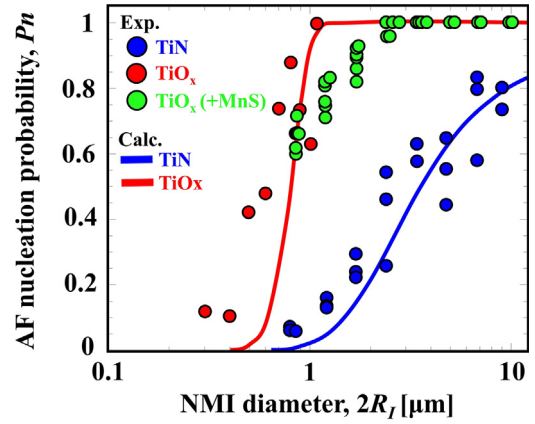


Fig. 3. Evolution of AF nucleation probability changed with NMI diameter. Experimental data come from Refs. [21–23]. Interfacial energies used to derive $\cos\theta_1$ are listed in Table 1.

the same size of d_i ($N_{nu,i}/N_{total,i}$). The reader is referred to Refs. [21–23] for more details. Such prediction for AF has not been reported in open literature. The measured data [21–23] come from low carbon ferroalloy with very close compositions, and therefore a same set of physical parameters are selected for calculations. The $\cos\theta_1$ values in individual cases with corresponding NMI type are derived from realistic interfacial energies [15,18,39] summarized in Table 1. Overall, the predicted P_n profiles are in consistent with observations. The P_n evolution changed with the increased NMI-diameter ($2R_l$) follows a sigmoidal tendency. As the NMI-size exceeds the AF-nucleation criterion (define as $P_n = 0.001$), P_n gradually grows within a rather narrow NMI-size range, followed by a sharp increasing with a continuous increment on the NMI-size. Afterwards, the growth gradient slows down and becomes insensitive to the NMI-size variation. When $\cos\theta_1$ increases from 0.26 (TiN) up to 0.42 (TiO_x), the critical $2R_l$ value for the AF-nucleation reduces from 0.6 to 0.4 μm. Meanwhile, a significant increasing of the P_n gradient is achieved. In the case of TiO_x, the P_n value approaches to 1 at a relatively small NMI-size (~1 μm). According to Ref. [15], the $\cos\theta_1$ value is negative for the pure case of MnS, resulting in $P_n \approx 0$ using the proposed model. For the case of TiO_x with certain amount of MnS, it is thus expected that the P_n increasing gradient should be smaller than that in the case of TiO_x. The measured spots of TiO_x + MnS inclusions are inserted into Fig. 3, and validate this speculation.

Based on the defined criterion (i.e. $P_n = 0.001$) for the AF-nucleation, the critical $2R_l$ value changed with $\cos\theta_1$ can be calcu-

lated, as is shown in Fig. 4. The evolution trend is in a hyperbolic shape. In the $\cos\theta_1 = 0$ condition, the critical $2R_l$ value equals 28 μm that is an excessive quantity in metallurgy point of view. Therefore, the assumption in Ricks model (i.e. $\sigma_{Iy} = \sigma_{I\sigma}$) [18] seems unrealistic. The common reported $\cos\theta_1$ value for an effective AF-nucleation is between ~ 0.2 and 0.6 [15] leading to a corresponding $2R_l$ range as $0.27\text{--}0.8 \mu\text{m}$. This prediction is quite close to the one ($= 0.5\text{--}0.8 \mu\text{m}$) suggested by Sarma et al. [6] through a comprehensive parameter study of experiments.

Using the HN case as the reference, the dimensionless nucleation energy, $\Delta G_{het}^*/\Delta G_{hom}^*$ and Zeldovich factor, Z_{het}/Z_{hom} are evaluated, as is shown in Fig. 5. The critical $2R_l$ value for the AF-nucleation from Fig. 4 is marked as well. The overall trend shows that the AF-NMI nucleation strength is quite close to the homogeneous nucleation as the NMI size is rather small. On the contrary, if the NMI size is sufficiently large, the AF-NMI nucleation strength will approach the heterogenous grain-boundary nucleation. According to Fig. 5(a), the nucleation energy reduces with the increased NMI-diameter. The decreasing gradient of TiO_x inclusion is larger than that of TiN inclusion. On the basis of thermodynamic, the AF-nucleation occurs at ΔG_{het}^* where $\frac{\partial(\Delta G)}{\partial R_l} = 0$. Nevertheless, NMI must also reach at its effective size. Thus, the AF-nucleation will take place only if the $\Delta G_{het}^*/\Delta G_{hom}^*$ ratio becomes smaller than 0.5. Below this boundary, the $\Delta G_{het}^*/\Delta G_{hom}^*$ decreasing gradient reduces gradually and approaches to quasi-constant state. In the range of $2R_l \leq 10 \mu\text{m}$, the TiO_x profile could cross through the GB-nucleation line, and the corresponding $2R_l$ value is $\sim 3.5 \mu\text{m}$. Based on Fig. 5(b), the Z_{het}/Z_{hom} ratio increases with the $2R_l$ increasing, and its critical value for the AF-nucleation is ~ 1.2 . Like $\Delta G_{het}^*/\Delta G_{hom}^*$, only the case of TiO_x inclusion could obtain a larger Z_{het}/Z_{hom} ratio than GB, while $2R_l$ has a different value as $\sim 8 \mu\text{m}$. The actual $2R_l$ value is determined as $\sim 4 \mu\text{m}$ according to the nucleation rate (J_n) that couples the ΔG_{het}^* and Z_{het} influences.

Although the critical NMI-diameter describes the boundary condition for the AF-nucleation, it does not provide information about the AF-nucleation potency. Based on the current section, a complex evolution of the AF-nucleation potency appears above this boundary, and is simultaneously influenced by the interfacial energies. To reveal these impacts from a more general perspective, we establish interaction maps of P_n and J_n , respectively, as is shown in Fig. 6. This is the core novelty in this section. It is interesting that the P_n distribution is ununiformed. The whole domain in Fig. 6(a) is mostly occupied by two regions as $P_n \leq 0.1$ and $P_n \geq 0.9$, which are located on the diagonal. Additionally, the larger the NMI-size

the wider the intermediate region ($0.1 < P_n < 0.9$). If the overall condition is near the $P_n = 0.1$ boundary, a small change on $\cos\theta_1$ (< 0.1) will be sufficient to considerably enhance the AF-nucleation probability. In the J_n aspect (see Fig. 6(b)), its distribution is much more uniform than that of J_n . The $P_n = 0.1$ line in Fig. 6(a) is inserted in Fig. 6(b). Even though the $P_n \leq 0.1$ boundary is quite narrow, a huge J_n difference is found in this area. It indicates that J_n is more sensitive to the variations of the interfacial energies and NMI-size, compared with P_n . As discussed in the introduction, diverse opinions exist in previous studies regarding the comparison of the AF-nucleation potency between GB and NMI. The J_n value in the GB-nucleation case is also plotted in Fig. 6(b). A region, in which NMI has a stronger AF-nucleation potency, is found (red colour region). In this region, the P_n value does not always equal 1 but is at least larger than 0.9. For the $2R_l < 10 \mu\text{m}$ range, the $\cos\theta_1$ value should be larger than ~ 0.49 . And this criterion raises with the NMI-size reduction. Thus, whether AF more easily nucleates on NMI or not depends on the superposition influences of θ_1 and $2R_l$. To sum up, Fig. 6 generates a novel and quantitative guideline for the AF-nucleation optimization.

3. Kinetics of AF anisotropy growth

3.1. Preliminary analysis using experimental observations

After nucleation, AF intends to precipitate with strong anisotropy in the γ matrix. Its growth behavior should be different from Widmanstätten due to the limited surface-area of the nucleation site (i.e. NMI). One important point, which no research mentioned before, is the misorientation of AF-favorable growth direction (FGD). Fig. 7 (a1)-(b1) schematically illustrates the initial AF-growth state. Here a NMI sphere is used as an approximation. If FGD and normal vector are parallel, the AF plate will follow an epitaxial precipitation from NMI (see Fig. 7(a1)). Theoretically, this is not always the case since the AF-nucleus locates randomly on NMI. When FGD and normal vector are not parallel, a misorientation angle (θ_m) appears and varies the interaction between AF and NMI, as is shown in Fig. 7(b1). Fig. 7(a2)-(b2) provide preliminary evidence of this speculation.

To further validate this statement, in situ observations of single AF-plate were conducted through the high temperature confocal laser scanning microscopy (HT-CLSM), as is shown in Fig. 8. A system of Fe-0.2 wt% C with the TiN addition is used as the model material at the temperature as 973 K. The reader is referred to Ref. [40] for more details of this technique. As mentioned, TiN is an effective NMI type to promote the AF-nucleation. In Fig. 8(a), the AF-plate grows epitaxially from NMI indicating that FGD and normal vector are almost parallel. Fig. 8(b) depicts the growth of an AF-plate with a certain misorientation angle. It is also noted that the region near NMI has a slight bending deformation marked with yellow arrow. Another example of the θ_m existence is provided by Fig. 8(c), in which the plate lengthening shows a double-way mode. With precipitation, NMI is gradually covered by the AF-plate. The results confirmed that the misorientation angle can exist and may influence the AF-evolution pathway. Nevertheless, it is difficult to rationalize the related mechanism purely from the experimental observations due to the complexity of the interface nature. In the subsequent section, we employ the multiphase-field modeling method to obtain a more comprehensive analysis.

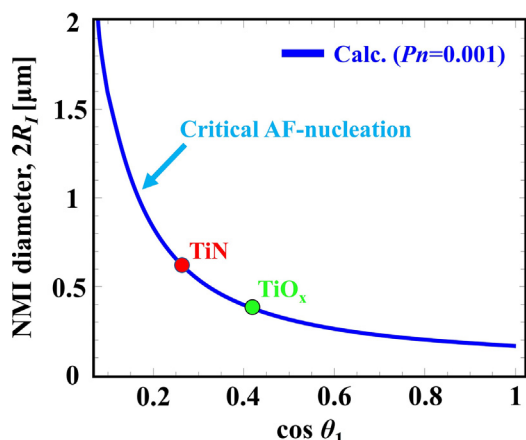


Fig. 4. Evolution of predicted critical NMI-diameter, $2R_l$ for AF-nucleation changed with $\cos\theta_1$.

3.2. Multiphase-field model description

3.2.1. Grand-potential formulation

In this section, we formulate a multiphase-field model (PFM) using the grand-potential approach proposed by Plapp [41]. The

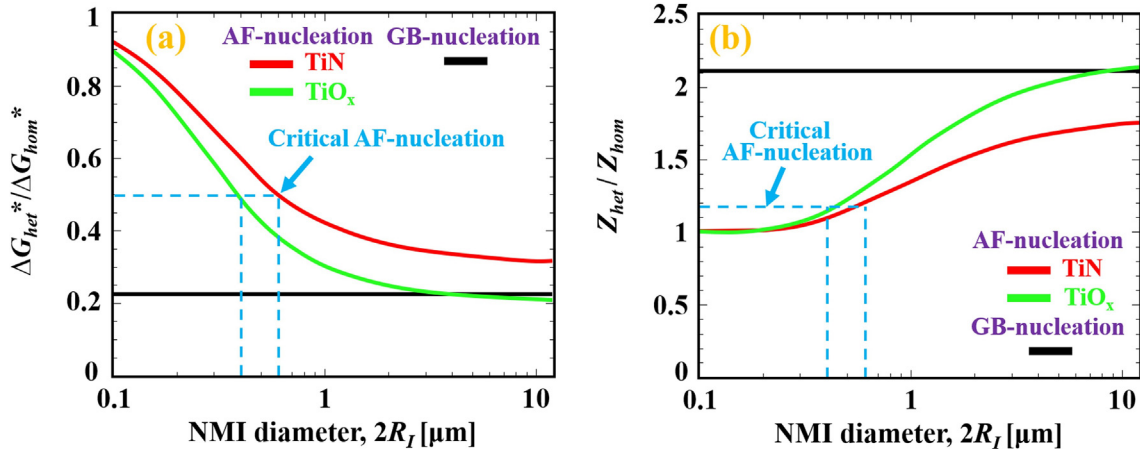


Fig. 5. Evolution of normalized (a) effective nucleation energy and (b) Zeldovich factor changed with NMI-diameter, $2R_I$.

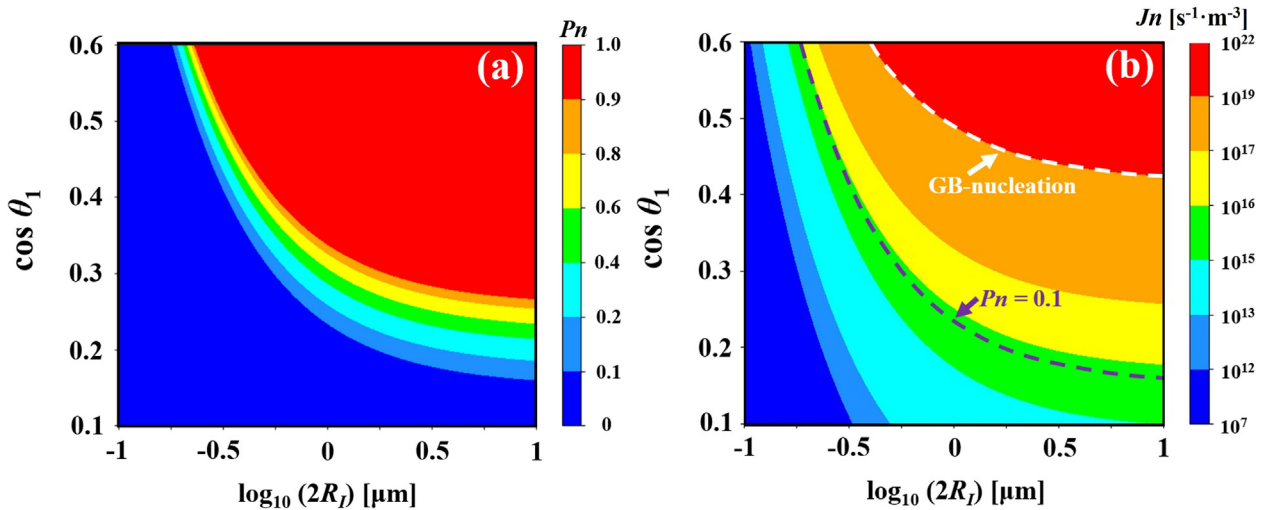


Fig. 6. Interaction map of (a) AF-nucleation probability, P_n ; (b) AF-nucleation rate, J_n .

model is on the basis of one paradigm that the AF formation is associated with carbon diffusion [42–43]. The individual phases are described using non-conserved order parameters $\eta = (\eta_1, \dots,$

$\eta_\beta, \dots, \eta_N)$. Meanwhile, the local composition of the conserved chemical species (A, B, \dots, K) is also needed to track the microstructure. Here $K-1$ independent variables are needed, and the K th species is the solvent. The driving force of the phase evolution is governed by the grand-potential (Ω) minimization. The grand-potential of the domain is defined as,

$$\Omega = \int (\omega_{bulk} + \omega_{int} + \omega_{el}) dV \quad (b1)$$

where ω_{bulk} , ω_{int} , ω_{el} are the contributions of the bulk grand-potential, interfacial energy and elastic energy, respectively. ω_{bulk} is formulated as,

$$\omega_{bulk} = \sum_{\beta=1}^N h_\beta \omega_\beta \quad (b2)$$

where $h_\beta = \eta_\beta^2 / \sum_{\beta=1}^N \eta_\beta^2$ denotes the interpolation function of the β phase, and ω_β is the β grand-potential density that gives [41],

$$\omega_\beta = \frac{G_\beta}{V_m} - \sum_{A=1}^{K-1} \mu_A X_\beta^A = f_\beta - \sum_{A=1}^{K-1} \mu_A X_\beta^A \quad (b3)$$

where G_β represents the Gibbs free energy of the β phase, V_m is the molar volume (assume a same constant for all phases), X_β^A is the molar fraction of chemical solute- A in the β phase, and μ_A is the diffusion potential of the solute- A . The Gibbs free energy of each phase

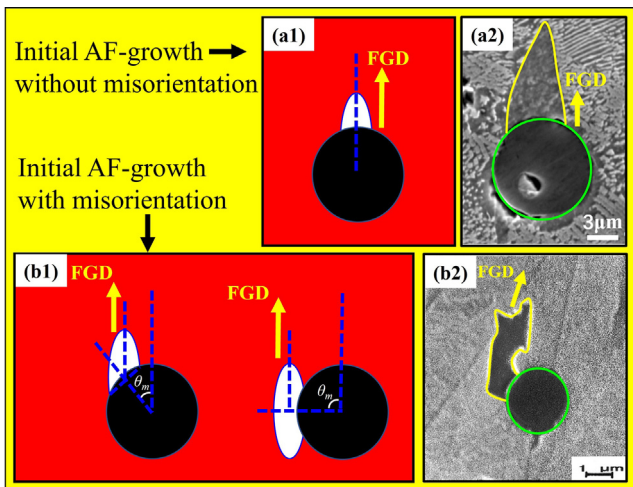


Fig. 7. (a1) Schematic illustration of initial AF-growth without misorientation; (a2) SEM-evidence of (a1); (b1) Schematic illustration of initial AF-growth with misorientation; (b2) SEM-evidence of (b1) [19]. Reproduced with permission [19]. Copyright 1999, Elsevier.

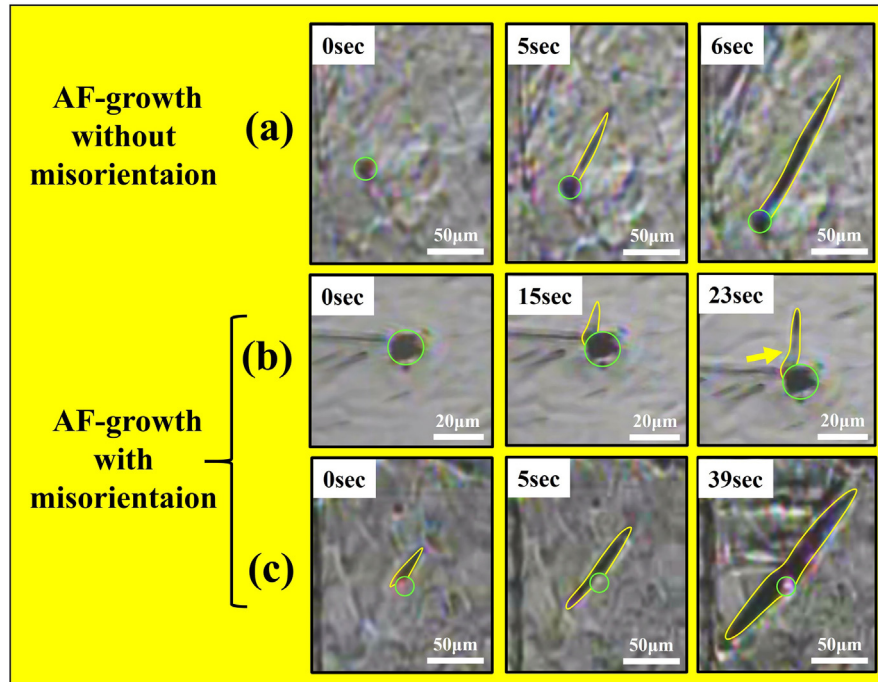


Fig. 8. In situ HT-CLSM observations of AF (yellow contour) formation at NMI (green contour). The yellow arrow marks the bending region. (For interpretation of the references to colour in this figure legend, the reader is referred to the web version of this article.)

is described using a parabolic approximation of the CALPHAD data [44] as,

$$G_\beta = G_{\beta,\min} + \sum_{A=1}^{K-1} \varepsilon_\beta^A (X_\beta^A - X_{\beta,\min}^{A,\min})^2 \quad (\text{b4})$$

where $G_{\beta,\min}$ is the minimum value of the Gibbs free energy, ε_β^A is related to the energy steepness, $X_{\beta,\min}^{A,\min}$ is the composition when the Gibbs free energy is minimum. The values of these parameters of the NMI solid bulk are set as $G_{NMI,\min} = -4 \times 10^4$ J/mol, $\varepsilon_{NMI}^C = 1.6 \times 10^7$ J/mol and $X_{NMI}^{C,\min} = 1 \times 10^{-10}$, respectively, to avoid the composition change of NMI during simulation. The diffusion potential (μ_A) is defined as,

$$\mu_A = \frac{\partial f_\beta}{\partial X_\beta^A} = \frac{2\varepsilon_\beta^A}{V_m} (X_\beta^A - X_{\beta,\min}^{A,\min}) \quad (\text{b5})$$

Coupling Eqs. (b3)-(b5) leads to a re-expressed form of ω_β as

$$\omega_\beta = \frac{G_{\beta,\min}}{V_m} - \sum_{A=1}^{K-1} \left(\frac{\mu_A^2 V_m}{4\varepsilon_\beta^A} + \mu_A X_{\beta,\min}^{A,\min} \right) \quad (\text{b6})$$

Using Eq. (b6), the phase concentration X_β^A reads,

$$X_\beta^A = -\frac{\partial \omega_\beta}{\partial \mu_A} = \frac{\mu_A V_m}{2\varepsilon_\beta^A} + X_{\beta,\min}^{A,\min} \quad (\text{b7})$$

Substituting Eq. (b7) into the overall concentration of the solute-A ($X_A = \sum_{\beta=1}^N h_\beta X_\beta^A$), the conversion relation between μ_A and X_A is explicitly achieved as,

$$\mu_A = \frac{X_A - \sum_{\beta=1}^N h_\beta X_{\beta,\min}^{A,\min}}{V_m \sum_{\beta=1}^N \frac{h_\beta}{2\varepsilon_\beta^A}} \quad (\text{b8})$$

The interfacial energy contribution (ω_{int}) is given by

$$\omega_{int} = \omega_{grad} + m$$

$$\cdot \left[\sum_{\beta=1}^N \left(\frac{\eta_\beta^4}{4} - \frac{\eta_\beta^2}{2} \right) + \frac{1}{2} \sum_{\beta=1}^N \left(\sum_{\delta=1}^N \gamma_{\beta\delta} \eta_\beta^2 \eta_\delta^2 \right) + \frac{1}{4} \right] \quad (\text{b9})$$

The first term in Eq. (b9) (ω_{grad}) represents the gradient energy contribution. Due to the crystallographic nature of most solids, the interfacial energy of precipitate-matrix is generally anisotropic. In this work, the anisotropy of the γ - α interfacial energy is considered. Meanwhile, it is approximated that the phase and concentration of NMI is not time dependent leading to the isotropy of the γ -NMI and α -NMI interfaces. To describe these features, the ω_{grad} term is given by,

$$\omega_{grad} = \frac{1}{2} k \left(|\nabla \eta_\alpha|^2 + |\nabla \eta_\gamma|^2 \right) + \frac{1}{2} \bar{k} |\nabla \eta_\alpha|^2 \quad (\text{b10})$$

where k denotes the gradient energy coefficient, and \bar{k} is the magnitude of k . Using the modified Yamanaka et al. model [45], k is expressed as follows,

$$k = \begin{cases} \bar{k} \cdot [Q_1 + Q_2 \cos(2\theta_s)]^2 \left[\frac{\cos(\theta_x)}{\cos(\theta_s)} \right]^2 & -\theta_s < \theta < \theta_s; \\ -\pi - \theta_s < \theta < -\pi + \theta_s; \pi - \theta_s < \theta < \pi + \theta_s \\ \bar{k} \cdot [Q_1 + Q_2 \cos(2\theta_x)]^2 & \text{other} \end{cases} \quad (\text{b11})$$

where Q_1 is the anisotropy scale (=2.0), Q_2 is the anisotropy strength (=1.25), θ_s is the smoothening angle ($=\pi/200$), θ_x is the difference between the orientation angle (θ) and reference angle ($\theta_0 = 90^\circ$). The second term in Eq. (b9) is a multiwell potential [46], m is a specific coefficient, $\gamma_{\beta\delta}$ are a set of constants related to the interfacial energy. By choosing the α - γ interface as the symmetric reference (i.e. $\gamma_{\alpha\gamma} = 1.5$), the values of \bar{k} and m are given by [47],

$$\bar{k} = 0.75 \sigma_{\alpha\gamma} W_{\alpha\gamma} \quad (\text{b12})$$

$$m = \frac{6\sigma_{\alpha\gamma}}{W_{\alpha\gamma}} \quad (\text{b13})$$

where $W_{\alpha\gamma}$ represents the characteristic α - γ interface width. The other $\gamma_{\beta\delta}$ values are determined through [48].

$$\gamma_{\beta\delta} = \frac{1}{(-5.288g^8 - 0.09364g^6 + 9.965g^4 - 8.183g^2 + 2.007)} \quad (\text{b14})$$

where $g = \sigma_{\beta\delta}/\sqrt{k m}$. Besides the interfacial energy, the misfit lattice parameters between the precipitate and corresponding parent phase generate the long-range elastic energy, which also contributes the interface anisotropy. The elastic influence coupled in the current PFM model is based on the theory framework of Khachaturyan [49] at small strains. The elastic strain energy is described using the classical equation of Hooke's law given by,

$$\omega_{el} = \frac{1}{2} \mathbf{C}_{ijkl} \mathbf{\epsilon}_{ij}^{el} \mathbf{\epsilon}_{kl}^{el} \quad (b15)$$

where \mathbf{C}_{ijkl} denotes the global elasticity tensor; $\mathbf{\epsilon}_{ij}^{el}$ represents the elastic strain, which read

$$\mathbf{C}_{ijkl} = \sum_{\beta}^N h_{\beta} \cdot \mathbf{C}_{ijkl}^{\beta} \quad (b16)$$

$$\mathbf{\epsilon}_{ij}^{el} = \mathbf{\epsilon}_{ij}^{tot} - \sum_{\beta}^N h_{\beta} \cdot \mathbf{\epsilon}_{ij}^{0,\beta} \quad (b17)$$

Principally, the total strain tensor ($\mathbf{\epsilon}_{ij}^{tot}$) and eigenstrain tensor ($\mathbf{\epsilon}_{ij}^{0,\beta}$) depend on both the concentration- and phase-field. Here we restrict ourselves to the case where these quantities are controlled by the functional of microstructure (order parameters). Due to the cubic crystal structures of all phases, the elasticity tensor ($\mathbf{C}_{ijkl}^{\beta}$) can be filled with constant isotropic symmetry,

$$\begin{bmatrix} 2\mu + \lambda & \lambda & \lambda & 0 & 0 & 0 \\ \lambda & 2\mu + \lambda & 2\mu + \lambda & 0 & 0 & 0 \\ \lambda & 2\mu + \lambda & 2\mu + \lambda & 0 & 0 & 0 \\ 0 & 0 & 0 & \mu & 0 & 0 \\ 0 & 0 & 0 & 0 & \mu & 0 \\ 0 & 0 & 0 & 0 & 0 & \mu \end{bmatrix} \quad (b18)$$

The Lamé constants μ ($=E/2(1+\nu)$) and λ ($=Ev/(1+\nu)(1-2\nu)$) are calculated using the corresponding Young's modulus (E) and Poisson ratio (ν). The values of E and ν are derived from the corresponding elasticity constants using *ab initio* methods [50–52]. Many orientation relationships (ORs) between the α variants and the γ parent matrix have been reported in literature. The most representative ORs in steels are Kurdjumow-Sachs (KS, i.e. $(1\ 1\ 1)_{\gamma}/(1\ 1\ 0)_{\alpha}$ and $[1\ 10]_{\gamma}/[1\ 11]_{\alpha}$) and Nishiyama-Wassermann (NW, i.e. $(1\ 1\ 1)_{\gamma}/(1\ 1\ 0)_{\alpha}$, $[1\ 10]_{\gamma}/[0\ 0\ 1]_{\alpha}$, $[11\ 2]_{\gamma}/[1\ 10]_{\alpha}$). The NW variants can be linked to the KS variants by a rotation angle as $\sim 5.26^\circ$ [53]. Meanwhile, the KS distortion matrix can be polarly decomposed into the theoretical Bain distortion and a corresponding rotation matrix [54]. Madariaga and gutiérrez [19] also reported that the OR between the AF and γ phase lies within the Bain region. Additionally, the OR between the TiN inclusion and α phase follows the Bain orientation [55]. Thus, the Bain distortion as a phenomenological state is applied to determine the eigenstrain of the γ - α -NMI system in the present study. Both the inclusion and γ phase are references, and the distortion matrix is based on the parent γ phase and is given in the reference coordinate basis (of vectors $[1\ 0\ 0]_{\gamma}$, $[0\ 1\ 0]_{\gamma}$, $[0\ 0\ 1]_{\gamma}$) as,

$$\begin{bmatrix} \frac{a_x}{a_{\gamma}} & 0 & 0 \\ 0 & \frac{\sqrt{2}a_z}{a_{\gamma}} & 0 \\ 0 & 0 & \frac{\sqrt{2}a_x}{a_{\gamma}} \end{bmatrix} \quad (b19)$$

where a_{α} ($=0.292$ nm [37]) and a_{γ} ($=0.354$ nm [37]) are the lattice parameters. The differences between the diagonal values and unity generate the eigenstrain tensor as,

$$\mathbf{\epsilon}_{ij}^{0,\alpha} = \begin{bmatrix} -0.18 & 0 & 0 \\ 0 & 0.17 & 0 \\ 0 & 0 & 0.17 \end{bmatrix} \quad (b20)$$

The elastic anisotropy based on Eq. (b20) is analyzed by generating a polar plot that describes the elastic energy distribution of a single α precipitate in a γ matrix, as is illustrated in Fig. 9. The angle denotes the relation between the vector normal to the α broad-face and X-axis. Four soft directions exist in the polar plot (marked with green arrows). The angle with the minimum elastic energy ($=44.6^\circ$ to Y-axis in the first quadrant) provides the highest driving force for the α growth. Up to date, it is still unclear that whether the elastic anisotropy has certain misorientation with respect to the interface anisotropy or not. More related study is required in future. In present work, it is postulated that the interface anisotropy and elastic anisotropy share a same tip-growth direction. Thus, the eigenstrain tensor needs to perform an anticlockwise rotation by 44.6° (see Fig. 9), and then the tip-growth direction is perpendicular to X-axis. The eigenstrain tensor is rotated through a rotation matrix (\mathbf{R}) about Z-axis according to Roe convention that is expressed as,

$$\mathbf{R} = \begin{bmatrix} \cos\omega & -\sin\omega & 0 \\ \sin\omega & \cos\omega & 0 \\ 0 & 0 & 1 \end{bmatrix} \quad (b21)$$

where ω represents the rotation angle ($=44.6^\circ$). The rotated eigenstrain tensor is determined by

$$\mathbf{\epsilon}_{ij}^{(0,\alpha)*} = \mathbf{R} \mathbf{\epsilon}_{ij}^{0,\alpha} \mathbf{R}^T = \begin{bmatrix} -0.0074 & -0.175 & 0 \\ -0.175 & -0.0026 & 0 \\ 0 & 0 & 0.17 \end{bmatrix} \quad (b22)$$

It is evident that the elastic influence is dominated by the shear component combined with much weaker dilatation.

3.2.2. Evolution equations

The evolution of each order parameter η_{β} is described using the time-dependent Ginzburg-Landau (TDGL) equation,

$$\frac{\partial \eta_{\beta}}{\partial t} = -L \frac{\delta \Omega}{\delta \eta_{\beta}} \quad (b23)$$

where δ is a functional derivative $\frac{\delta}{\delta \eta_{\beta}} = \frac{\partial}{\partial \eta_{\beta}} - \nabla \cdot \frac{\partial}{\partial \nabla \eta_{\beta}}$, L denotes the phase mobility coefficient that is defined as,

$$L = L_{x\gamma}^{h_{x\gamma}} \cdot L_{z\alpha}^{h_{z\alpha}} \cdot L_{y\gamma}^{h_{y\gamma}} \quad (b24)$$

where $L_{x\gamma}$, $L_{z\alpha}$ and $L_{y\gamma}$ are the mobility coefficients of the α - γ , NMI- α and NMI- γ interfaces, respectively. The $L_{z\alpha}$ and $L_{y\gamma}$ values are set extremely small to avoid the NMI evolution. The interpolation function of the interface takes the form,

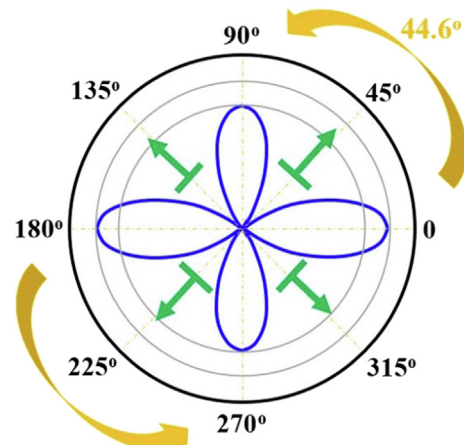


Fig. 9. Polar plot of the elastic energy distribution of a α precipitate in γ matrix.

$$h_{\beta\delta} = \frac{\eta_\beta^2 \eta_\delta^2}{\sum_\beta \sum_{\delta \neq \beta} \eta_\beta^2 \eta_\delta^2} \quad (\text{b25})$$

The evolution of each solute species is expressed through a generalized diffusion equation as [56],

$$\frac{\partial X_A}{\partial t} = \nabla \cdot \left(\sum_{B=1}^{K-1} M_{AB} \nabla \mu_B \right) \quad (\text{b26})$$

where M_{AB} is the mass mobility coefficient between the solute- A and - B . If the interdiffusion is neglected, Eq. (b26) can be simplified to,

$$\frac{\partial X_A}{\partial t} = \nabla \cdot (M_{AA} \nabla \mu_A) \quad (\text{b27})$$

Following the same form of L , M_{AA} is expressed using an interpolation function of mobilities in individual phases (M_{AA}^α) as,

$$M_{AA} = M_{AA}^{\alpha, h_\alpha} \cdot M_{AA}^{\gamma, h_\gamma} \cdot M_{AA}^{\zeta, h_\zeta} \quad (\text{b28})$$

An extremely small M_{AA}^I is applied to prevent the composition evolution of NMI. Since the overall concentration X_A is related to both μ_A and η . (see Eq. (b8)), its derivative can be expanded using the chain rule and is given by,

$$\nabla X_A = \sum_{B=1}^{K-1} \frac{\partial X_A}{\partial \mu_B} \nabla \mu_B + \sum_{\beta=1}^N \frac{\partial X_A}{\partial \eta_\beta} \nabla \eta_\beta \quad (\text{b29})$$

By defining the $\frac{\partial X_A}{\partial \mu_B}$ term as S_{AB} ($S_{AB} = 0$ when $A \neq B$), Eq. (b29) is rearranged as,

$$\nabla \mu_A = S_{AA}^{-1} \left(\nabla X_A - \sum_{\beta=1}^N \frac{\partial X_A}{\partial \eta_\beta} \nabla \eta_\beta \right) \quad (\text{b30})$$

The derivative of X_A by η_β reads,

$$\frac{\partial X_A}{\partial \eta_\beta} = \frac{\partial}{\partial \eta_\beta} \sum_{\delta=1}^N h_\delta X_{\delta A} = \sum_{\delta=1}^N X_{\delta A} \left(\frac{\partial h_\delta}{\partial \eta_\beta} \right) \quad (\text{b31})$$

Substituting Eqs. (b30)-(31) into Eq. (b27), we obtain the explicit equation of the concentration evolution as,

$$\begin{aligned} \frac{\partial X_A}{\partial t} &= \nabla \cdot \left(M_{AA} S_{AA}^{-1} \nabla X_A \right) - \nabla \\ &\cdot \left\{ M_{AA} S_{AA}^{-1} \sum_{\beta=1}^N \left[\sum_{\delta=1}^N X_{\delta A} \left(\frac{\partial h_\delta}{\partial \eta_\beta} \right) \right] \nabla \eta_\beta \right\} \end{aligned} \quad (\text{b32})$$

Using Eq.(b7) and $X_A = \sum_{\beta=1}^N h_\beta X_{\beta A}$, S_{AA} is expressed as,

$$\begin{aligned} S_{AA} &= \sum_{\beta=1}^N h_\beta S_{AA}^\beta = \sum_{\beta=1}^N h_\beta \left(\frac{\partial X_{\beta A}}{\partial \mu_A} \right) \\ &= \sum_{\beta=1}^N h_\beta \left(\frac{\partial}{\partial \mu_A} \left(\frac{\mu_A V_m}{2 \mathcal{E}_{\beta A}} + X_{(\beta, \min) A} \right) \right) = V_m \sum_{\beta=1}^N \frac{h_\beta}{2 \mathcal{E}_{\beta A}} \end{aligned} \quad (\text{b33})$$

3.2.3. Simulation set-up

Two simulation strategies exist for Widmanstätten type microstructure research in previous studies. For the first type, the interface width is set based on its physically realistic quantity, which is in a nano-scale [57–59]. In this case, the domain is limited to a relatively small size range. In the second type, the domain size is comparable with the realistic microstructure [60]. However, a much thicker interface width must be selected to balance the computation capacity. Here we choose the first strategy in this work. The numerical investigation of the AF growth on NMI is in 2D which fits the shape-feature of the AF thin plate. The model material is the Fe-0.2 wt%TiN ternary system under an isothermal condition ($T = 973$ K), and the parameters used for the simulation are summarized in Table 2. The domain size is 200×800 nm. The

interface width (5 nm) includes 5 grids to get a sufficient resolution. The NMI particle is defined as a sphere with the radius as 20 nm. A small AF partial-ellipsoid with the aspect-ratio as 1/3 and equivalent radius as 8 nm is placed on NMI at the initial stage. Three different misorientation angles (see the illustration in Fig. 7) as 0, 30° and 90° are selected for the analysis. All PFM simulations are performed using the open-source-code framework MOOSE [61], and the results are visualized with the open-source software ParaView [62].

3.3. Evaluation of AF-evolution process

To verify the PFM-model authenticity in Section 3.2, we compare various morphologies of the AF-plates observed by SEM in the Fe-0.2 wt%TiN system with the PFM simulations using different θ_m . The exemplary microstructures for the qualitative comparison are shown in Fig. 10. According to Fig. 10 (a1), two separated AF-plates at a same NMI exhibit quite similar morphologies and follow a rotationally symmetrical correlation. This microstructure is most likely formed through multiple nucleus. Each plate has certain bending deformation. The widest part of each plate is not located at the contact region with NMI rather some distance towards NMI. The simulated AF-plate with $\theta_m = 0$ at the time 15.6 ms (see Fig. 10 (a2)) well reproduces this behavior. Fig. 10 (b1) presents an AF-plate with double-way extension and needle-point tips. Applying $\theta_m = 90^\circ$ for simulation (at the time 31.1 ms), a same AF-plate type is obtained as is shown in Fig. 10 (b2). The AF-plate in Fig. 10 (c1) shows a more irregular morphology. The region above NMI looks like a projection of ‘wine bottle’. The left-hand side near the bottom region has a lower curvature than that on the right-hand side. Additionally, a shorter and sharper tip bypasses NMI along an opposite direction. All these features are reasonably captured by the simulation with $\theta_m = 30^\circ$ at the time 17.3 ms (see Fig. 10 (c2)). We also identify an interesting type of the AF-plate microstructure, as illustrated in Fig. 10 (d1). It can be seen that the tip region of the marked plate looks like a ‘straight-back blade’ including a straight spine and an edge that curves up to meet it at the tip top. Using $\theta_m = 30^\circ$ (see Fig. 10 (d2)), the simulated AF-plate at the time 31.1 ms shows a same tip type. In a short summary, the simulated microstructures using the current PFM model present a high similarity with the experimental observations.

Fig. 11 presents the evolution of the AF-plate contour in its precipitation process. The dash lines denote the AF-phase boundaries

Table 2
Physical parameters applied in the current PFM model.

Symbol	Definition and unit	Value
T	Temperature [K]	973
R_g	Gas constant [J/(mol·K)]	8.3145
V_m	Molar volume [m^3/mol]	7×10^{-6}
W_{xy}	Reference interface width [nm]	5
$\sigma_{x\gamma}$	Interfacial energy between α and γ [J/m^2]	0.75 [18]
$\sigma_{l\gamma}$	Interfacial energy between NMI and γ [J/m^2]	0.636 [39]
$\sigma_{l\alpha}$	Interfacial energy between NMI and α [J/m^2]	0.439 [39]
M_{CC}^I	Mass mobility coefficient of carbon in γ [$\text{m}^5/(\text{J}\cdot\text{s})$]	1.9×10^{-25}
M_{CC}^{α}	Mass mobility coefficient of carbon in α [$\text{m}^5/(\text{J}\cdot\text{s})$]	1×10^{-23}
M_{CC}^{NMI}	Mass mobility coefficient of carbon in NMI [$\text{m}^5/(\text{J}\cdot\text{s})$]	1×10^{-90}
$L_{x\gamma}$	Mobility coefficient of $\alpha\text{-}\gamma$ interface [$\text{m}^3/(\text{J}\cdot\text{s})$]	3×10^{-7}
$L_{l\gamma}$	Mobility coefficient of NMI- γ interface [$\text{m}^3/(\text{J}\cdot\text{s})$]	1×10^{-90}
$L_{l\alpha}$	Mobility coefficient of NMI- α interface [$\text{m}^3/(\text{J}\cdot\text{s})$]	1×10^{-90}
E_γ	Young's modulus of γ [GPa]	191.6 [50]
E_α	Young's modulus of α [GPa]	226.5 [51]
E_{NMI}	Young's modulus of NMI [GPa]	418.7 [52]
v_γ	Poisson ratio of γ	0.295 [50]
v_α	Poisson ratio of α	0.349 [51]
v_{NMI}	Poisson ratio of NMI	0.32 [52]

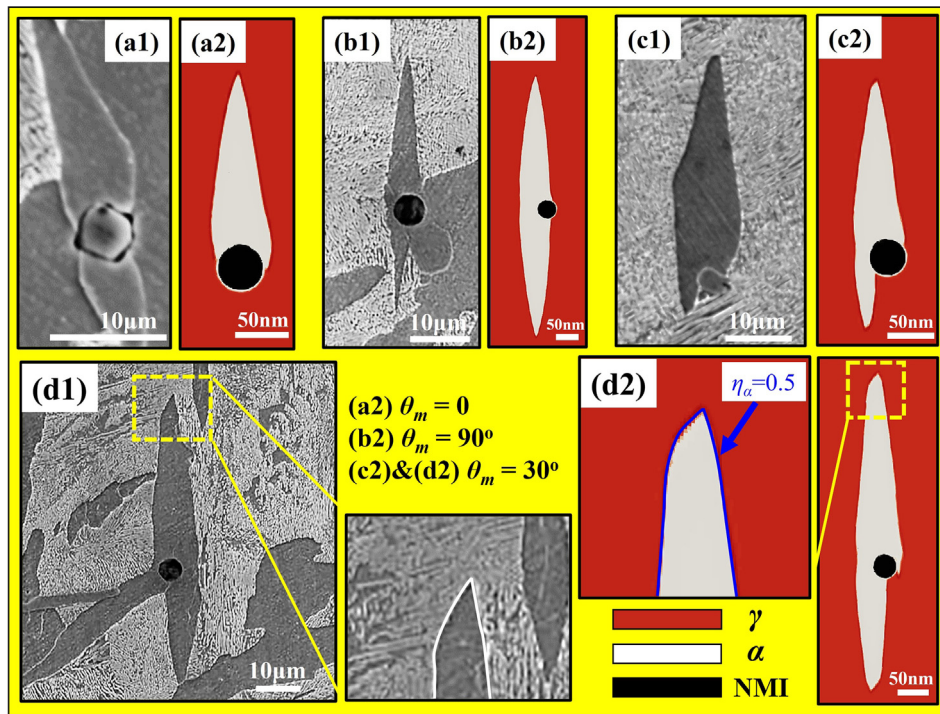


Fig. 10. Comparison of the AF-morphologies between the ex-situ SEM observations ((a1)-(d1)) and PFM simulations ((a2)-(d2)).

with the level set of $\eta_\alpha = 0.5$ at different time-points. In the $\theta_m = 0$ case (see Fig. 11(a)), the plate displays a needle-point tip and a slightly asymmetric morphology at the early stage. As the precipitation continuous, the tip gradually deflects to the right-hand side and transforms to a 'straight-back blade' shape. At the same time, the widened plate bypasses NMI on the opposite direction and then follows a double-way lengthening. For the newly formed tips, the region on the right-hand side grows little bit faster than the region on the left-hand side. Both tips have deformation in different degrees. When θ_m equals 30° (see Fig. 11(b)), the growth tendency is quite similar with the case of $\theta_m = 0$. Due to the misorientation angle, the region on the left-hand side easily bypasses NMI on the opposite direction. The newly formed tip is almost in rotational symmetry with the initial tip. The deformed

tips are not as sharp as those in the $\theta_m = 0$ case. As the plate covers the right-hand side of NMI, a new tip appears on the opposite direction. For the $\theta_m = 90^\circ$ case (see Fig. 11(c)), the plate grows in mirror symmetry based on NMI. The tips maintain the needle-point shape during the plate evolution. It is interesting to mention that there is bending near the NMI region in all three cases (see the zoomed images). Some locations have convex curvatures and some other locations exhibit concave curvatures. The simulated phenomena well reproduce the experimental observations (see Figs. 8 and 10). It indicates the important impacts of the θ_m and AF-NMI interface on the AF-evolution kinetics.

To understand the carbon evolution during the AF-growth, an example of the carbon distribution at the time as 8.7 ms for the $\theta_m = 0$ case along the vertical-direction (passing the AF tip) and horizontal-direction (passing the widest region of AF) is shown in Fig. 12(a). Overall speaking, the concentration peak is identified for both directions. During the AF precipitation, carbon atoms are diffused from the newly formed AF into the austenite matrix, resulting in a carbon accumulation at the interface. Such build-up phenomenon inhibits the AF growth kinetics. It is found that the distribution behavior of carbon concentration along two different directions are quite different. For the AF-tip region, the corresponding carbon peak (molar fraction) and diffusion length are 0.015 and 6.3 nm, respectively. On the other hand, a higher carbon peak (~ 0.028) and a longer diffusion length (~ 23.6 nm) are obtained for the widest side of AF. It indicates that the carbon atoms number of the former related to the migration is relatively smaller than that of the latter one. Thus, the interface of the tip region is able to more quickly migrate. The time-dependent variations of the max. carbon concentration and diffusion length are given in Fig. 12(b) and Fig. 12(c), respectively. For the AF side-region, both the carbon accumulation and diffusion length increase with the time increment, limiting the AF widening. However, for the AF tip-region, the carbon accumulation only shows a slight increasing, and the diffusion length almost remains stable with time. It again shows the stronger lengthening behavior at the tip.

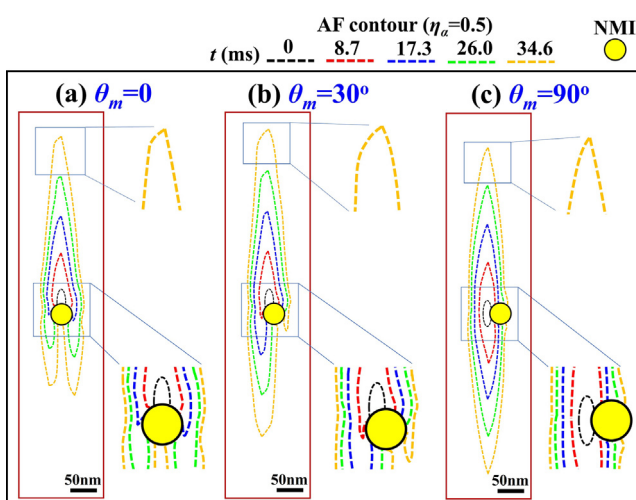


Fig. 11. Dynamic evolution of the AF-plate contour ($\eta_\alpha = 0.5$) with the misorientation angle as a) $\theta_m = 0$, b) $\theta_m = 30^\circ$ and c) $\theta_m = 90^\circ$.

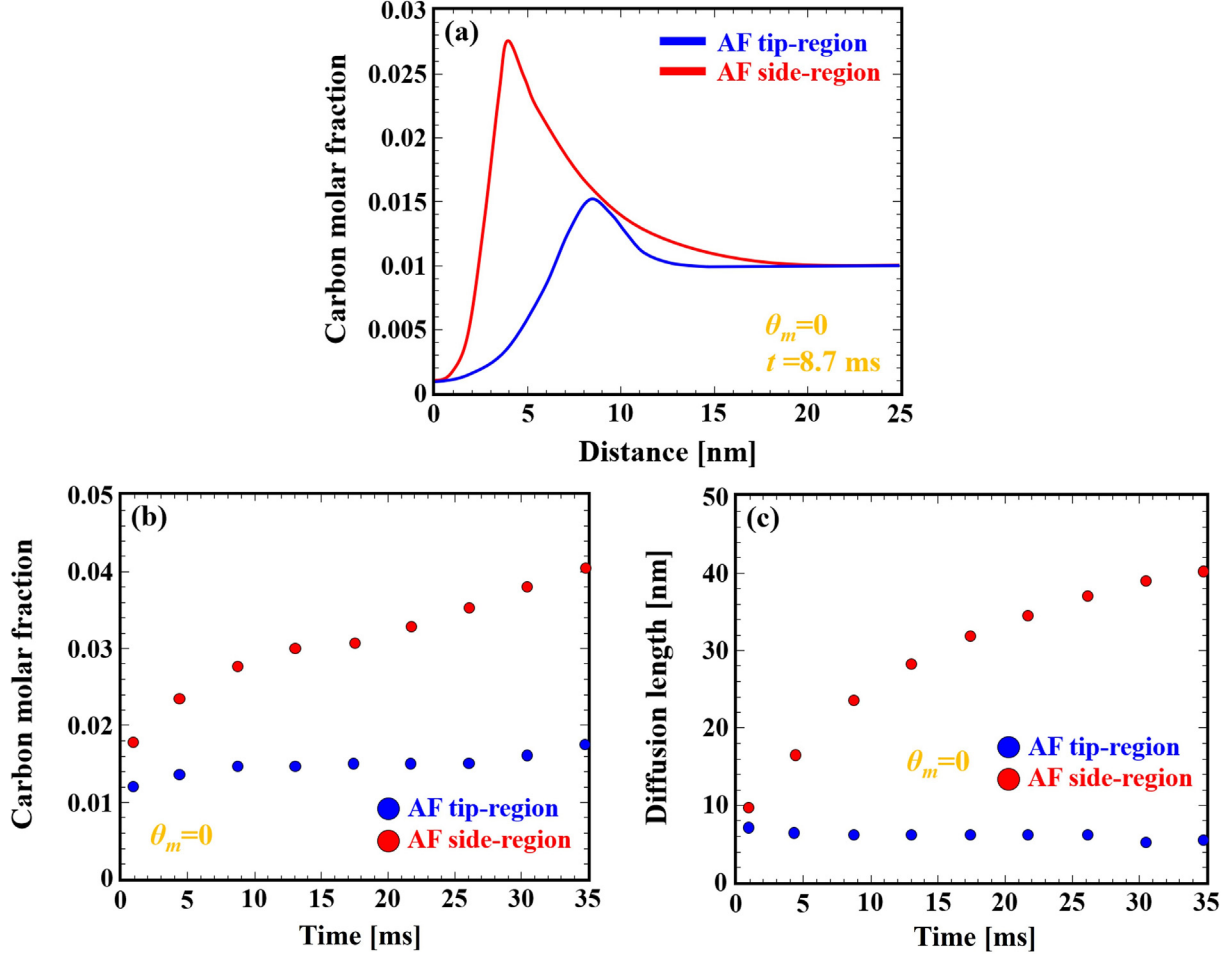


Fig. 12. (a) Carbon distribution at the time 8.7 ms for the $\theta_m = 0$ case. Evolution of (b) max. carbon concentration and (c) diffusion length with the time variation.

To further elucidate the AF-evolution in Fig. 11, Fig. 13 presents the stress fields (i.e. σ_{xx} , σ_{yy}) with different orientation angles (θ_m) at the time 34.6 ms. In all cases, high magnitudes of each stress components locate near the AF-tips and AF-NMI interface. For the regions near the tips, the magnitude of the σ_{yy} component is significantly higher in comparison to the σ_{xx} component. Even though the σ_{yy} distribution near the tips obeys rotational symmetry in all cases, the σ_{yy} magnitude and distribution possess diverse behaviors. When $\theta_m = 0$, the tensile stresses at the site of tip1 are more broadly distributed than the compressive stresses, as is shown in Fig. 13(b). This relation corresponds to the asymmetry of the elastic energy (see Fig. 9). The AF-curvature on the compressive site is larger than that on the tensile site forming the tip bending to the right. The tensile stress field at the tip2 site and the compressive stress field at the tip3 site are similar with those of tip1 (see Fig. 13(g)-(h)). However, the stress fields on the right site of tip2 and left site of tip3 weaken because of their elimination-interaction. For the tip2 case, the magnitude and distribution discrepancies between the tensile- and compressive stress field enlarges leading to the tip bending to the left. In the tip3 case, the weakened tensile stresses become lower in magnitude than the compressive stresses resulting in the tip bending to the right. As θ_m equals 30° (see Fig. 13(d) and 13(i)), the asymmetry degree of the stress fields on both sides of each tip reduces although the tensile stress field remains broader. The quasi-symmetric magnitude and distribution of the stress fields at the tip sites are achieved when the θ_m value further increases up to 90°

(Fig. 13(f) and 13(j)). As the result, the AF-plate has needle-point tips on both sides.

Unlike the tip-regions, the σ_{xx} magnitude presents a comparable level with the σ_{yy} component near the AF-NMI interface. The anisotropy of the elastic energy results in the ununiformed stress field. The σ_{xx} component distribution of this region is given in Fig. 14. The magnitude and distribution of the stress field vary during the AF-precipitation. Even though the AF-contours with different θ_m have very different shapes and evolution behaviors, a general pattern of such complexity is identified. It is found that the curvature variation of the AF-contour agrees well to the distribution of the stress field. A widening process is facilitated at the site with relatively higher stress magnitude (marked with 'white arrows'). In contrast, a weaker widening corresponds to the soft region (marked with 'black arrows'). A more detailed example is provided by Fig. 15. It shows that the stress field can induce an alternating distribution of these two widening behaviors on the AF-plate, which in turn, generates a wave contour.

The growth kinetics of the AF-plate is further analyzed by tracking the evolution of max. length (L_{max}) and max. width (W_{max}), as is shown in Fig. 16. It has been reported that the growth of Widmanstätten type microstructure obeys linear lengthening and parabolic widening [42,58]. Apparently, this trend cannot precisely explain the AF growth despite their high formation similarity. The AF-evolution shows a more complicated behavior, and both the lengthening and widening are influenced by θ_m . From the lengthening perspective (see Fig. 15(a)), the evolution trend of $\theta_m = 0$ is

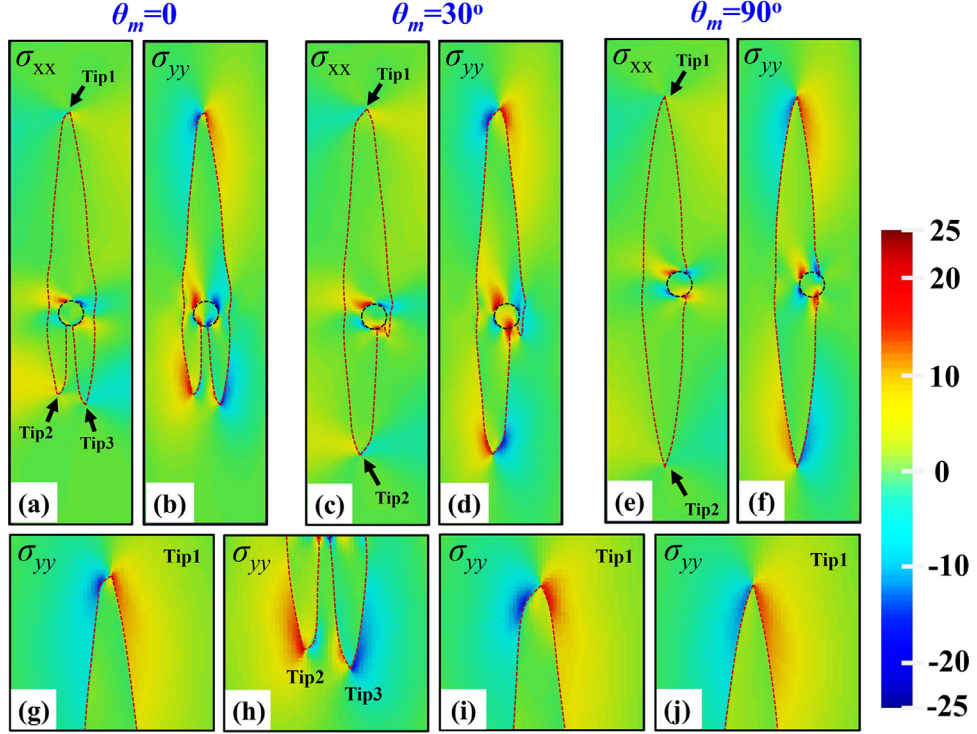


Fig. 13. Stress fields of the AF-plate with the misorientation angle as (a)-(b) $\theta_m = 0$, (c)-(d) $\theta_m = 30^\circ$ and (e)-(f) $\theta_m = 90^\circ$. (g)-(h) are stress fields of the tip-regions in (b), (i) and (j) are stress fields of the tip1-regions in (d) and (f), respectively. The colorbar unit is 1.16GPa.

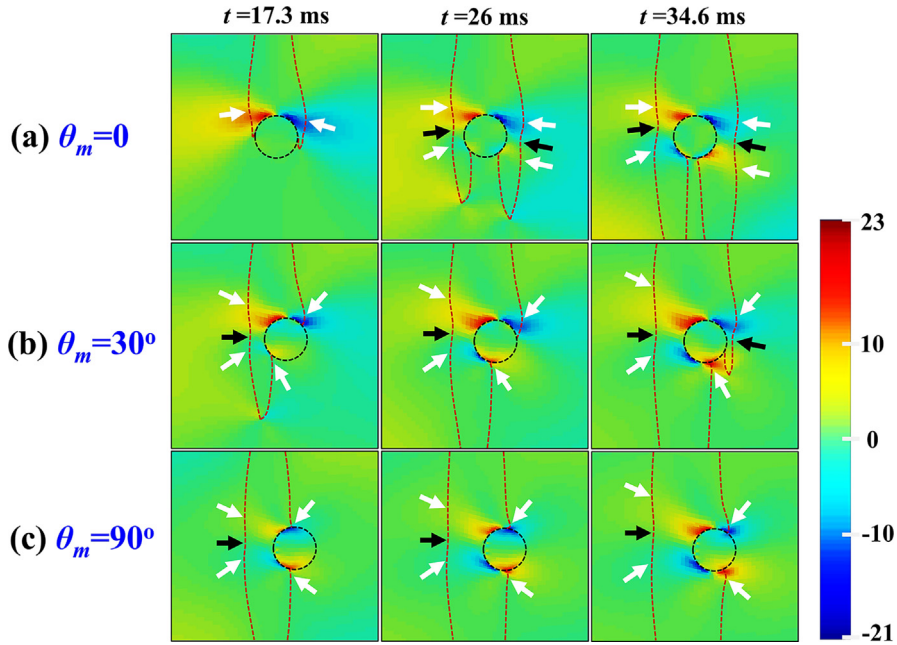


Fig. 14. Evolution of the σ_{xx} fields around NMI with the misorientation angle as a) $\theta_m = 0$, b) $\theta_m = 30^\circ$ and c) $\theta_m = 90^\circ$. The colorbar unit is 1.16GPa.

in parabolic shape. A transient period, in which the lengthening rate smoothly increases, exists with the time increasing. The reason is that the AF-plate starts to bypass NMI in the opposite direction. In this situation, the growth mode changes from single-way to double-way. The simulated AF-contour at the normalized time as 0.5 in Fig. 16(a) describes this particular moment. The lengthening rate becomes constant once such period completes. The trend curvature reduces when the θ_m value increases to 30° , while the tran-

sient period still exists (see the AF-contour at the normalized time as 0.25 in Fig. 15(a)). For $\theta_m = 90^\circ$, the trend becomes linear since the growth mode (i.e. double-way) keep the same during the precipitation. As for the widening aspect (see Fig. 16(b)), the simulated data of $\theta_m = 0$ and $\theta_m = 30^\circ$ almost overlap with each other, and follow a parabolic tendency denoting a reduced widening rate with the increased time. When the θ_m value becomes 90° , the data points almost follow a linear relation instead of a parabolic rela-

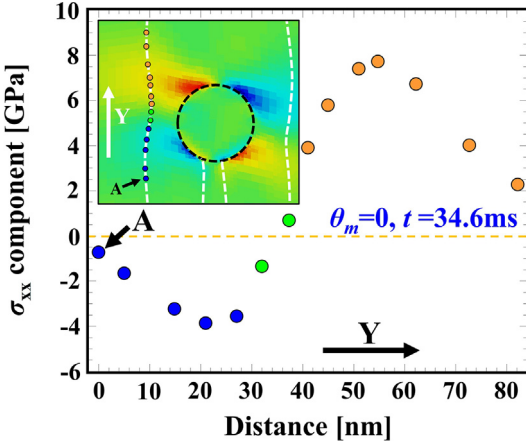


Fig. 15. σ_{xx} component distribution on the AF-contour with $\theta_m = 0$ at the time as 34.6 ms.

tion. Fig. 16(c)-(d) compare the simulated results (yellow regions come from Fig. 16(a)-(b)) with the experimental data from the measurement using HT-CLSM images. The PFM modeling reasonably describes the evolution tendency of the experimental AF-size although deviations exist. There are several possible limiting

factors leading to such deviations. In the current work, NMI is approximated as a sphere, and only one NMI-size is selected for simulation. It is known that NMI can have different morphologies (e.g. sphere, polygon, etc.) and different sizes from tens of nanometers to tens of microns. Also, the eigenstrain tensor applied here is the theoretical Bain distortion for a phenomenological study. In addition, the plastic relaxation, which is not included in the current model, may accompany during the AF-precipitation. Consequently, more future work is still desired to provide a better quantitative prediction of the AF formation from the NMI surface.

4. Conclusions

In this work we focus on the kinetics of the heterogenous nucleation and anisotropic growth of acicular ferrite (AF) plate from the non-metallic inclusion (NMI) surface. The main motivation is to propose new insights about the AF-precipitation mechanisms. The most important conclusions are summarized below:

- 1) A CNT model has been developed to account for the heterogeneous AF-nucleation on NMI. The model has been parameterized to agree with experimental data in the open literature. It shows that the evolution of the nucleation probability (P_n) changed with the NMI-diameter ($2R_l$) follows a sigmoidal tendency. The correlation between the critical $2R_l$ for AF-

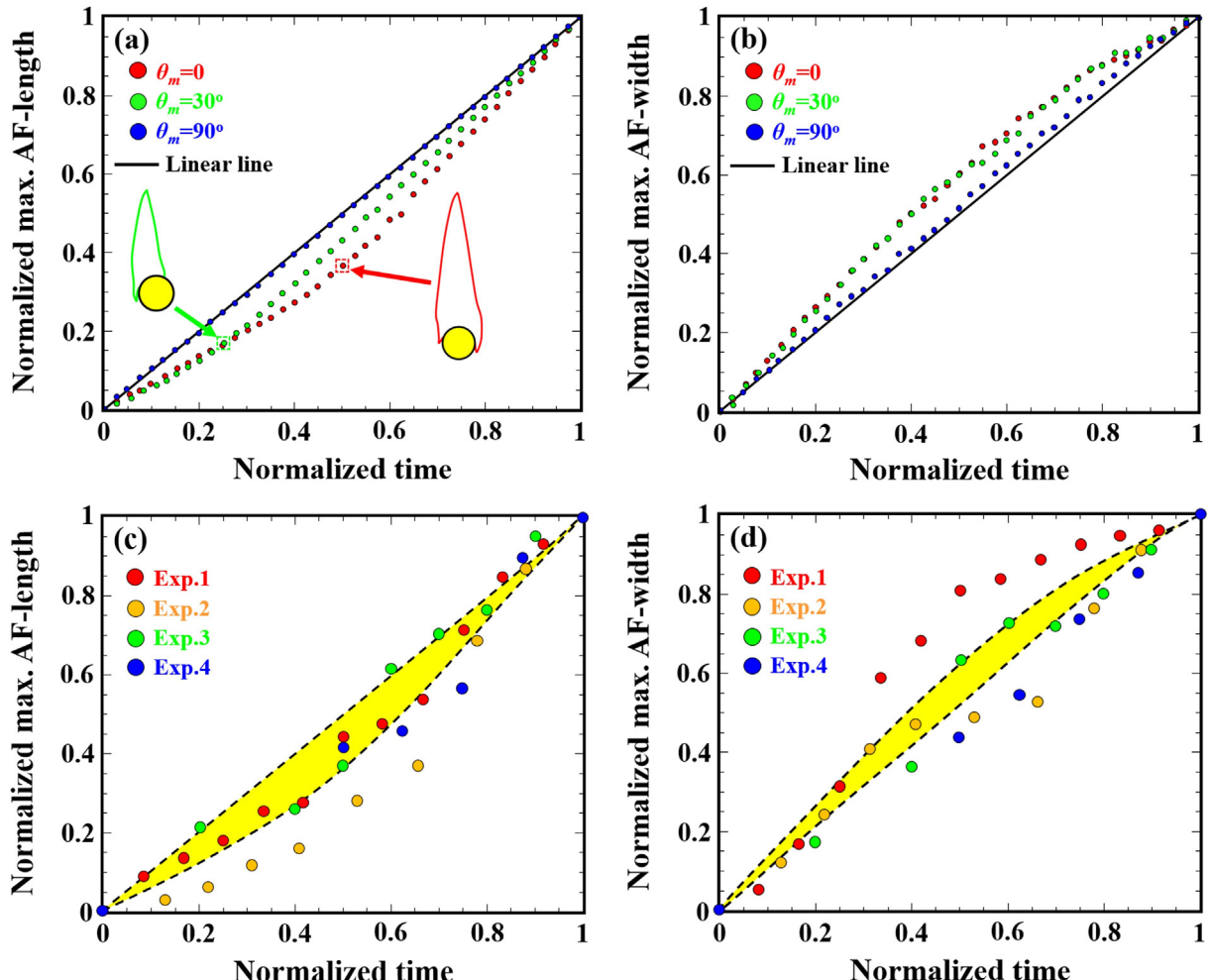


Fig. 16. Simulated evolution of the (a) max. length and (b) max. width of AF-plate with time. Comparison of (c) max. length and (d) max. width of AF-plate between the simulation (marked with yellow regions) and experimental observations. (For interpretation of the references to colour in this figure legend, the reader is referred to the web version of this article.)

- nucleation and overall interfacial energies (representing by $\cos\theta_1$) is in a hyperbolic shape. And the critical $2R_t$ range is suggested as 0.27 to 0.8 μm .
- 2) Based on the proposed CNT model, an interaction map is for the first time established to quantitatively predict the superposition influences of the interfacial energies and NMI-size on the AF-nucleation potency. It clarifies the possibility that the AF-nucleation potency can be stronger than that of grain boundary (GB).
 - 3) A multiphase-field model (PFM) using grand potential approach is formulated to describe the AF-evolution process after nucleation. The synergy between the PFM-modeling and experimental observations is achieved. At current stage, the proposed CNT model for nucleation is not incorporated with the proposed PFM model for growth. For future study, a further development of PFM is desired to capture the continuous process from heterogenous nucleation to growth.
 - 4) It is validated that the misorientation angle (θ_m) between the favorable growth direction (FGD) and normal vector exists and influences the AF-evolution behavior. The tip can be transformed from the needle-point shape to the bending shape (e.g. 'straight-back blade') by the mere θ_m variation. The key mechanism is to control the asymmetry degree of the stress field at the AF-tip site.
 - 5) The interaction at the AF-NMI interface between AF and NMI has an important influence on the AF-evolution. The anisotropic stress field induced by such interaction leads to the irregular AF-deformation near NMI.
 - 6) Lengthening and widening behaviors of AF during its growth are more complicated than those of Widmanstätten type microstructure. By varying θ_m , the evolution profile of lengthening and widening with time can transform from a parabola to a linear line.

Declaration of Competing Interest

The authors declare that they have no known competing financial interests or personal relationships that could have appeared to influence the work reported in this paper.

Acknowledgement

WM would like to acknowledge the Swedish Foundation for International Cooperation in Research and Higher Education (STINT, Project No. PT2017-7330 & IB2020-8781) and Jernkontoret (The Swedish Steel Producers' Association), in particular, Axel Ax:son Johnsons forskningsfond, Prytziska fonden nr 2, and Gerhard von Hofstens Stiftelse för Metallurgisk forskning for the financial support.

References

- [1] X. Fu, X.-D. Wang, B. Zhao, Q. Zhang, S. Sun, J.-J. Wang, W. Zhang, L. Gu, Y. Zhang, W.-Z. Zhang, W. Wen, Z.e. Zhang, L.-Q. Chen, Q. Yu, E.n. Ma, Atomic-scale observation of non-classical nucleation-mediated phase transformation in a titanium alloy, *Nat. Mater.* 21 (3) (2022) 290–296, <https://doi.org/10.1038/s41563-021-01144-7>.
- [2] P.R. Rios, E. Villa, Transformation kinetics for inhomogeneous nucleation, *Acta Mater.* 57 (4) (2009) 1199–1208, <https://doi.org/10.1016/j.actamat.2008.11.003>.
- [3] S.E. Offerman, N.H. Van Dijk, J. Sietsma, S. Grigull, E.M. Lauridsen, L. Margulies, H.F. Poulsen, M.T. Rekvdelt, S. Van der Zwaag, Grain nucleation and growth during phase transformations, *Science* 298 (5595) (2002) 1003–1005. <https://www.science.org/doi/10.1126/science.1076681>.
- [4] L. Cheng, K.M. Wu, New insights into intragranular ferrite in a low-carbon low-alloy steel, *Acta Mater.* 57 (13) (2009) 3754–3762, <https://doi.org/10.1016/j.actamat.2009.04.045>.
- [5] R.A. Farrar, P.L. Harrison, Review Acicular ferrite in carbon-manganese weld metals: an overview, *J. Mater. Sci.* 22 (11) (1987) 3812–3820, <https://doi.org/10.1007/BF01133327>.
- [6] D.S. Sarma, A.V. Karasev, P.G. Jönsson, On the role of non-metallic inclusions in the nucleation of acicular ferrite in steels, *ISIJ Int.* 49 (7) (2009) 1063–1074, <https://doi.org/10.2355/isijinternational.49.1063>.
- [7] H. Adrian, F. B. Pickering, Effect of titanium additions on austenite grain growth kinetics of medium carbon V-Nb steels containing 0.008–0.018%N, *Mater. Sci. Tech.* 7 (2) (1991) 176–182 <https://doi.org/10.1179/mst.1991.7.2.176>.
- [8] C. Bernhard, J. Reiter, H. Presslinger, A model for predicting the austenite grain size at the surface of continuously-cast slabs, *Metal. Mater. Trans. B* 39 (6) (2008) 885–895, <https://doi.org/10.1007/s11663-008-9197-8>.
- [9] W. Mu, H. Shibata, P. Hedström, P.G. Jönsson, K. Nakajima, Ferrite formation dynamics and microstructure due to inclusion engineering in low-alloy steels by Ti_2O_3 and TiN addition, *Metal. Mater. Trans. B* 47 (4) (2016) 2133–2147, <https://doi.org/10.1007/s11663-016-0630-0>.
- [10] D. Loder, S.K. Michelic, C. Bernhard, Acicular ferrite formation and its influencing factors-A Review, *J. Mater. Sci. Res.* 6 (1) (2017) 24–43, <https://doi.org/10.5539/jmsr.v6n1p24>.
- [11] J.-H. Shim, Y.W. Cho, S.H. Chung, J.-D. Shim, D.N. Lee, Nucleation of intragranular ferrite at Ti_2O_3 particle in low carbon steel, *Acta Mater.* 47 (9) (1999) 2751–2760, [https://doi.org/10.1016/S1359-6454\(99\)00114-7](https://doi.org/10.1016/S1359-6454(99)00114-7).
- [12] W. Mu, Microstructure and inclusion characteristics in steels with Ti-oxide and TiN additions, Doctoral thesis, KTH, (2015) <http://kth.diva-portal.org/smash/record.jsf?pid=diva2%3A797693&dswid=2451>.
- [13] J.-H. Shim, Y.-J. Oh, J.-Y. Suh, Y.W. Cho, J.-D. Shim, J.-S. Byun, D.N. Lee, Ferrite nucleation potency of non-metallic inclusions in medium carbon steels, *Acta Mater.* 49 (12) (2001) 2115–2122, [https://doi.org/10.1016/S1359-6454\(01\)00134-3](https://doi.org/10.1016/S1359-6454(01)00134-3).
- [14] J.-S. Byun, J.-H. Shim, Y.W. Cho, D.N. Lee, Non-metallic inclusion and intragranular nucleation of ferrite in Ti-killed C-Mn-steel, *Acta Mater.* 51 (6) (2003) 1593–1606, [https://doi.org/10.1016/S1359-6454\(02\)00560-8](https://doi.org/10.1016/S1359-6454(02)00560-8).
- [15] W. Mu, P.G. Jönsson, K. Nakajima, Prediction of intragranular ferrite nucleation from TiO_2 , TiN and VN inclusions, *J. Mater. Sci.* 51 (4) (2016) 2168–2180, <https://doi.org/10.1007/s10853-015-9527-6>.
- [16] H. K. D. H. Bhadeshia, Possible effects of stress on steel weld microstructures, Mathematical modelling of weld phenomena, eds H. Cerjak, H. Bhadeshia, Institute of materials, London, (1995) 71–118 <https://www.phase-trans.msm.cam.ac.uk/2005/Graz2/Graz2.html>.
- [17] N.H. Fletcher, Size effect in heterogenous nucleation, *J. Chem. Phys.* 29 (3) (1958) 572–576, <https://doi.org/10.1063/1.1744540>.
- [18] R.A. Ricks, P.R. Howell, G.S. Barritte, The nature of acicular ferrite in HSLA steel weld metals, *J. Mater. Sci.* 17 (3) (1982) 732–740, <https://doi.org/10.1007/BF00540369>.
- [19] I. Madariaga, I. Gutiérrez, Role of the particle-matrix interface on the nucleation of acicular ferrite in a medium carbon microalloyed steel, *Acta Mater.* 47 (3) (1999) 951–960, [https://doi.org/10.1016/S1359-6454\(98\)00388-7](https://doi.org/10.1016/S1359-6454(98)00388-7).
- [20] T. Furuhara, J. Yamaguchi, N. Sugita, G. Miyamoto, T. Maki, Nucleation of proeutectoid ferrite on complex precipitates in austenite, *ISIJ Int.* 43 (10) (2003) 1630–1639, <https://doi.org/10.2355/isijinternational.43.1630>.
- [21] W. Mu, P.G. Jönsson, H. Shibata, K. Nakajima, Inclusion and microstructure characteristics in steels with TiN additions, *Steel Res. Int.* 87 (3) (2016) 339–348, <https://doi.org/10.1002/srin.201500061>.
- [22] T.K. Lee, H.J. Kim, B.Y. Kang, S.K. Hwang, Effect of inclusion size on the nucleation of acicular ferrite in welds, *ISIJ Int.* 40 (12) (2000) 1260–1268, <https://doi.org/10.2355/isijinternational.40.1260>.
- [23] W. Mu, P.G. Jönsson, K. Nakajima, Effect of sulfur content on inclusion and microstructure characteristics in steels with Ti_2O_3 and TiO_2 additions, *ISIJ Int.* 54 (12) (2014) 2907–2916, <https://doi.org/10.2355/isijinternational.54.2907>.
- [24] S.S. Babu, S.A. David, Inclusion formation and microstructure evolution in low alloy steel welds, *ISIJ Int.* 42 (12) (2002) 1344–1353, <https://doi.org/10.2355/isijinternational.42.1344>.
- [25] G.I. Rees, H.K.D.H. Bhadeshia, Bainite transformation kinetics Part1 modified model, *Mater. Sci. Tech.* 8 (11) (1992) 985–993, <https://doi.org/10.1179/mst.1992.8.11.985>.
- [26] S.S. Babu, The mechanism of acicular ferrite in weld deposits, *Curr. Opin. Solid State Mater. Sci.* 8 (3–4) (2004) 267–278, <https://doi.org/10.1016/j.cosscsm.2004.10.001>.
- [27] I. Madariaga, J.L. Romero, I. Gutiérrez, Upper acicular ferrite formation in a medium-carbon microalloyed steel by isothermal transformation: nucleation enhancement by CuS, *Metal. Mater. Trans. A* 29 (13) (1998) 1003–1015, <https://doi.org/10.1007/s11661-998-1009-x>.
- [28] X. Wan, K. Wu, G. Huang, R. Wei, In situ observations of the formation of fine-grained mixed microstructures of acicular ferrite and bainite in the simulated coarse-grained heated-affected zone, *Steel Res. Int.* 85 (2) (2014) 243–250, <https://doi.org/10.1002/srin.201200313>.
- [29] D. Zhang, H. Terasaki, Y. Komizo, In situ observation of the formation of intragranular acicular ferrite at non-metallic inclusions in C-Mn steel, *Acta Mater.* 58 (4) (2010) 1369–1378, <https://doi.org/10.1016/j.actamat.2009.10.043>.
- [30] D. Loder, S.K. Michelic, A. Mayerhofer, C. Bernhard, On the capability of nonmetallic inclusions to act as nuclei for acicular ferrite in different steel grades, *Metal. Mater. Trans. B* 48 (4) (2017) 1992–2006, <https://doi.org/10.1007/s11663-017-0984-y>.

- [31] K.C. Russell, Nucleation in solids: The induction and steady state effects, *Ad. Collo. Inter. Sci.* 13 (3–4) (1980) 205–318, [https://doi.org/10.1016/0001-8686\(80\)80003-0](https://doi.org/10.1016/0001-8686(80)80003-0).
- [32] G.I. Rees, H.K.D.H. Bhadeshia, Thermodynamics of acicular ferrite nucleation, *Mater. Sci. Tech.* 10 (5) (1994) 353–358, <https://doi.org/10.1179/mst.1994.10.5.353>.
- [33] M. Tong, D. Li, Y. Li, J. Ni, Y. Zhang, Monte Carlo-method simulation of the deformation-induced ferrite transformation in the Fe-C system, *Metal. Mater. Trans. A* 35 (5) (2004) 1565–1577, <https://doi.org/10.1007/s11661-004-0263-9>.
- [34] L.H. Van Vlack, Intergranular energy of iron and some iron alloys, *JOM* 3 (3) (1951) 251–259, <https://doi.org/10.1007/BF03397307>.
- [35] E. Clouet, Modeling of nucleation processes, *ASM Handbook Vol. 22A, Fundamentals of modeling for metals processing*, ASM Int. 22A (2009) 203–219 <https://hal.archives-ouvertes.fr/hal-00449858v2>.
- [36] S.-J. Lee, D.K. Matlock, C.J.V. Tyne, An empirical model for carbon diffusion in austenite incorporating alloying element effects, *ISIJ Int.* 51 (11) (2011) 1903–1911, <https://doi.org/10.2355/isijinternational.51.1903>.
- [37] J.D. Watson, P.G. McDougall, The crystallography of Widmanstätten ferrite, *Acta Metall.* 21 (7) (1973) 961–973, [https://doi.org/10.1016/0001-6160\(73\)90153-3](https://doi.org/10.1016/0001-6160(73)90153-3).
- [38] M. Lazaridis, M. Kulmala, B.Z. Gorbunov, Binary heterogenous nucleation at a non-uniform surface, *J. Aerosol Sci.* 23 (5) (1992) 457–466, [https://doi.org/10.1016/0021-8502\(92\)90017-P](https://doi.org/10.1016/0021-8502(92)90017-P).
- [39] Z.G. Yang, C. Zhang, T. Pan, The mechanism of intragranular ferrite nucleation on inclusion in steel, *Mater Sci Forum* 475–479 (2005) 113–116, <https://doi.org/10.4028/www.scientific.net/MSF.475-479.113>.
- [40] W. Mu, P. Hedström, H. Shibata, P.G. Jönsson, K. Nakajima, High-temperature confocal laser scanning microscopy studies of ferrite formation in inclusion-Engineered steels: a review, *JOM* 70 (10) (2018) 2283–2295, <https://doi.org/10.1007/s11837-018-2921-1>.
- [41] M. Plapp, Unified derivation of phase-field models for alloy solidification from a grand-potential functional, *Phy. Rev. E* 84 (3) (2011), <https://doi.org/10.1103/PhysRevE.84.031601> 031601.
- [42] M. Hillert, L. Höglund, J. Ågren, Diffusion-controlled lengthening of Widmanstätten plates, *Acta Mater.* 51 (7) (2003) 2089–2095, [https://doi.org/10.1016/S1359-6454\(03\)00008-9](https://doi.org/10.1016/S1359-6454(03)00008-9).
- [43] A. Borgenstam, M. Hillert, J. Ågren, Metallographic evidence of carbon diffusion in the growth of bainite, *Acta Mater.* 57 (11) (2009) 3242–3252, <https://doi.org/10.1016/j.actamat.2009.03.026>.
- [44] P. Gustafson, A Thermodynamic Evaluation of the Fe-C System, *Scand. J. Metall.* 14 (1985) 259–267.
- [45] A. Yamanaka, T. Takaki, Y. Tomita, Phase-field simulation of austenite to ferrite transformation and Widmanstätten ferrite formation in Fe-C alloy, *Mater. Trans.* 47 (11) (2006) 2725–2731, <https://doi.org/10.2320/matertrans.47.2725>.
- [46] N. Moelans, A quantitative and thermodynamically consistent phase-field interpolation function for multi-phase systems, *Acta Mater.* 59 (3) (2011) 1077–1086, <https://doi.org/10.1016/j.actamat.2010.10.038>.
- [47] N. Moelans, B. Blanpain, P. Wollants, Quantitative analysis of grain boundary properties in a generalized phase field model for grain growth in anisotropic systems, *Phy. Rev. B* 78 (2) (2008), <https://doi.org/10.1103/PhysRevB.78.024113> 024113.
- [48] L.K. Aagesen, Y. Gao, D. Schwen, K. Ahmed, Grand-potential-based phase-field model for multiple phases, grains, and chemical components, *Phy. Rev. E* 98 (2) (2018), <https://doi.org/10.1103/PhysRevE.98.023309>.
- [49] A.G. Khachaturyan, *Theory of Structural Transformations in Solids*, Wiley, New York, 1983.
- [50] B. Hutchinson, M. Malmström, J. Lönnqvist, P. Bate, H. Ehteshami, P.A. Korzhavyi, Elasticity and wave velocity in fcc iron (austenite) at evaluated temperatures- experimental verification of *ab-initio* calculations, *Ultrasronics* 87 (2018) 44–47, <https://doi.org/10.1016/j.ultras.2018.02.009>.
- [51] M. Souissi, H. Numakura, Elastic properties of Fe-C and Fe-N martensites, *ISIJ Int.* 55 (7) (2015) 1512–1521, <https://doi.org/10.2355/isijinternational.55.1512>.
- [52] P. Steneteg, O. Hellman, O.Y. Vekilova, N. Shulumba, F. Tasnádi, I.A. Abrikosov, Temperature dependence of TiN elastic constants from ab initio molecular dynamic simulations, *Phy. Rev. B* 87 (9) (2013), <https://doi.org/10.1103/PhysRevB.87.094114> 094114.
- [53] H. K. D. H. Bhadeshia, Possible effects of stress on steel weld microstructures, *Mathematical modelling of weld phenomena*, eds H. Cerjak, H. Bhadeshia, Institute of materials, London, (1995) 71–118 <https://www.phase-trans.msm.cam.ac.uk/2005/Graz2/Graz2.html>.
- [54] C. Cayron, Continuous atomic displacements and lattice distortion during fcc-bcc martensitic transformation, *Acta Mater.* 96 (2015) 189–202, <https://doi.org/10.1016/j.actamat.2015.06.010>.
- [55] A.R. Mills, G. Thewlis, J.A. Whiteman, Nature of inclusions in steel weld metals and their influence on formation of acicular ferrite, *Materials Science and Technology* 3 (12) (1987) 1051–1061, <https://doi.org/10.1179/mst.1987.3.12.1051>.
- [56] J.-O. Andersson, J. Ågren, Models for numerical treatment of multicomponent diffusion in simple phases, *J. App. Phys.* 72 (4) (1992) 1350–1355, <https://doi.org/10.1063/1.351745>.
- [57] I. Loginova, J. Ågren, G. Amberg, On the formation of Widmansättten ferrite in binary Fe-C phase field approach, *Acta Mater.* 52 (13) (2004) 4055–4063, <https://doi.org/10.1016/j.actamat.2004.05.033>.
- [58] P.G.K. Amos, E. Schoof, D. Schneider, B. Nestler, Chemo-elastic phase-field simulation of the cooperative growth of mutually-accommodating Widmansättten plates, *J. Alloys. Comp.* 767 (2018) 1141–1154, <https://doi.org/10.1016/j.jallcom.2018.07.138>.
- [59] C. Lin, J. Wan, H. Ruan, Phase field modelling of Widmanstätten ferrite formation in steel, *J. Alloys. Comp.* 769 (2018) 620–630, <https://doi.org/10.1016/j.jallcom.2018.07.372>.
- [60] A. Bhattacharya, K. Ankit, B. Nestler, Phase-field simulations of curvature-induced cascading of Widmanstätten-ferrite plates, *Acta Mater.* 123 (2017) 317–328, <https://doi.org/10.1016/j.actamat.2016.10.035>.
- [61] C.J. Permann, D.R. Gaston, D. Andriš, R.W. Carlsen, F. Kong, A.D. Lindsay, J.M. Miller, J.W. Peterson, A.E. Slaughter, R.H. Stogner, R.C. Martineau, MOOSE: Enabling massively parallel Multiphysics simulation, *SoftwareX* 11 (2020) 100430, <https://doi.org/10.1016/j.softx.2020.100430>.
- [62] Ayachit, Utkarsh, The ParaView Guide: A Parallel Visualization Application, Kitware, 2015, ISBN 978-1930934306 <https://www.paraview.org/>.